2017

Plasma Property Estimation from Dual-Wavelength Interferometry

Andrew J. Hamilton
Wright State University

Repository Citation

Hamilton, Andrew J., "Plasma Property Estimation from Dual-Wavelength Interferometry" (2017). *Browse all Theses and Dissertations*. 1772.
https://corescholar.libraries.wright.edu/etd_all/1772

Plasma Property Estimation from Dual-Wavelength Interferometry

A thesis submitted in partial fulfillment
of the requirements for the degree of
Master of Science in Engineering

by

Andrew J. Hamilton
B.S.E.E., Wright State University, 2013

2017
Wright State University

Wright State University
Graduate School

May 28, 2017

I HEREBY RECOMMEND THAT THE THESIS PREPARED UNDER MY SUPERVISION BY Andrew J. Hamilton ENTITLED Plasma Property Estimation from Dual-Wavelength Interferometry BE ACCEPTED IN PARTIAL FULFILLMENT OF THE REQUIREMENTS FOR THE DEGREE OF Master of Science in Engineering.

Michael A. Saville, Ph.D., P.E.
Thesis Director

Brian D. Rigling, Ph.D.
Chair, Department of Electrical Engineering

Committee on
Final Examination

Michael A. Saville, Ph.D., P.E.

Amit R. Sharma, Ph.D.

Vladimir I. Sotnikov, Ph.D.

Robert E. W. Fyffe, Ph.D.
Vice President for Research and
Dean of the Graduate School

ABSTRACT

Hamilton, Andrew J. M.S. EGR., Department of Electrical Engineering, Wright State University, 2017. *Plasma Property Estimation from Dual-Wavelength Interferometry.*

Diagnostics are necessary for measurement of plasma parameters such as electron, ion and atomic densities, electron temperature, plasma expansion velocity and spatial resolution of density gradients. These parameters play a critical role in defining how a plasma will interact with electromagnetic radiation. For example, the plasma black-out phenomenon occurs when electromagnetic waves are at frequencies below the plasma frequency, where plasma frequency is a function of electron density. Wave propagation diagnostics can improve understanding of a plasma when measurement supports parameter estimation. In this report, the dual-wavelength interferometry method provides a single diagnostic capability to measure plasma expansion velocity, atomic density and electron densities. Using a laboratory plasma created with wire-ablation pulsed-power techniques and the Sarkisov model [1], electron densities and atomic densities are estimated for copper and aluminum plasmas.

Table of Contents

List of Figures

List of Tables

Acknowledgement

I would like to take this opportunity to extend my thanks to many people, whom without their help, none of this work would have been possible. First and foremost, my advisor Dr. Michael Saville. I have always looked up to and respected him from the very first time I was sitting in his class. The time we have spent together going over the details of this project from conceptual thoughts to completion has not been wasted and will endure my lifetime. Though some details may have seemed trivial to me, he showed how important that each and every detail can be. The final thing I will take away is to always resort to first principles. He would not accept anything but my best, and for that I thank him.

Additionally, I would like to thank Dr. Amit Sharma for his time and for being on my advisory committee. Dr. Vladimir Sotnikov, my sponsor for this effort and team lead at work, has been a technical mentor for several years. Without his guidance and desire to aid in my growth as a young engineer, I would not have been successful.

James Caplinger has been very helpful through MATLAB routines and providing a better understanding of the physics behind this effort. Bob Schueler provided exceptional support in the laboratory through optical alignment, LabView and downright good discussion on what I was trying to do.

My girlfriend Shanel Fultz has been extremely supportive of me during this effort, even though she didn't get the quality time she deserved. Without her help and support, I would have gone to work with 2 different shoes, an empty belly, and many spelling and grammatical errors.

There are many more to thank, including my technical advisor, Dr. Bae-Ian Wu, and management for allowing and encouraging me to do this work. I hope that I won't let them down. To all others not mentioned here, I extend my fullest and complete gratitude.

Dedication

This thesis is dedicated to my parents George and Sue Hamilton. They raised me to be a respectful and hardworking man, even though many times they doubted any existence of that. Additionally, I would like to acknowledge my late grandfather William T. Bergedick for setting a good example and showing me the finer things in life...golf, tennis and hard work.

Introduction

1.1 Motivation

It is estimated that 99% of all matter in the universe is in the plasma state [2]. Plasma is the fourth state of matter and is found in a gaseous-like state comprised of many ionized particles, free electrons, and neutral particles contained in electrostatic fields, magnetostatic fields and/or electromagnetic fields. Plasma's existence on earth, though rare, can be observed in lightning, neon signs, fluorescent lighting, Aurora Borealis, Aurora Australis and laboratory experiments [3]. An improved understanding of plasma is critical to understanding how modern communications, radar and telemetry will interact in the presence of plasma [3]. It has been found that different diagnostics measuring the same plasma parameter differ by up to a factor of 10 [3]. This error is unacceptable for applying mitigation techniques of radio frequency (RF) transmission [4, 5, 6, 7]. Plasma physics has recently experienced significant growth in all of these categories with the computational advancement of memory, processing capabilities and simulation methods [3], yet, measurement methods are critical for validation.

Light interference, as first described by Robert Hooke in the late 17th century, explains the phenomenon observed when fringes develop after light reflects from two glass surfaces between a thin air film [8]. This initial observation of fringe lines provided validation for Hooke to present a wave theory of light accounting for the periodicity of fringe lines. This theory was opposed by Newton due to his beliefs in wave theory being unable to describe rectilinear propagation or polarization, but was later put into6 present form by Huyghens in 1690 [8]. It was not until Young's double slit experiment in 1801, when the wave nature of light was accepted in the scientific community [8]. In this experiment, Young demonstrated that light from a single source, traveling through two separate pinholes, and viewed on an opaque surface would create fringe lines where the waves of light overlapped [9].This is due to constructive and destructive interference of the phase. Deriving from Young's work, significant advances in interferometry have yielded validation of empirical standards, measurements of wavelengths, frequency and Doppler information, distance, displacement and astrophysical information [10]. In 1896, Michelson used interferometry to measure the wavelength of the red Cd line and verify the accuracy of the Pt-Ir bar (International Standard of the meter at that time) [8]. After the execution of these classical experiments, it became apparent that interferometry was a useful diagnostic for precision measurements.

Single-wavelength interferometry is commonly used as a laboratory measurement to measure electron densities of a plasma, but dual-wavelength has been suggested for plasma measurements [11, 12]. Propagating waves from a probing laser through a frequency doubling crystal yields two independent, coherent waves during the laser pulse. This polychromatic pulse is suitable for a dual-wavelength measurement.

Dual-wavelength interferometry is our proposed diagnostic that can be used to measure plasma expansion velocity, atomic densities and electron densities in a laboratory plasma. This diagnostic will produce two measurements, collected at the same moment in time, providing both temporal and spatial information about the ionization process occurring during wire ablation. Furthermore, development of this technique will utilize the same equipment as a single-wavelength interferometry measurement and require only an additional camera and beam splitter.

Following the Sarkisov model for atomic and electron densities, fringe shift measurements enable plasma property analysis [1].

$$\delta(y) = \frac{2\pi\alpha}{\lambda} \int N_a dx - 4.49 \times 10^{-14} \lambda \int N_e dx \tag{1.1}$$

Of interest here is Eq. (1.1), this theoretical model will provide the technique to estimate both atomic and electron densities.

1.2 Challenges

The biggest challenges are measurement repeatability and interferometry analysis due to the turbulent nature of plasma. The wire ablation technique forms a temporally-varying plasma. Therefore, the plasma behavior must be observed from creation to dissipation.

Measurement repeatability requires planning and strict following of established procedures to complete each experiment. Secure and precise placement of the optics is necessary before alignment. Multiple devices are connected together and require proper timing for the experiments to be successful. Sample preparation, handling and placement are considerations that cannot be ignored. A checklist is utilized for each experiment to ensure no procedures are missed.

The output from an experiment utilizing optical interferometry as a diagnostic, is an image known as an interferogram. Interferograms represent measured data in fringes. One set of both dark and light fringes represents a periodic shift due to the phase difference between two coherent light sources [8]. Interferometric images containing a plasma region, as found in our work, will have several fringes, with fringe shifts in the plasma region. The distance a fringe shifts is proportional to atomic and electron densities [1]. These interferograms will need to be analyzed through computer algorithms or manually measured to extract the fringe information. There are many codes available for this, but are very costly [13]. A simple method to extract the fringe information is developed during this research effort.

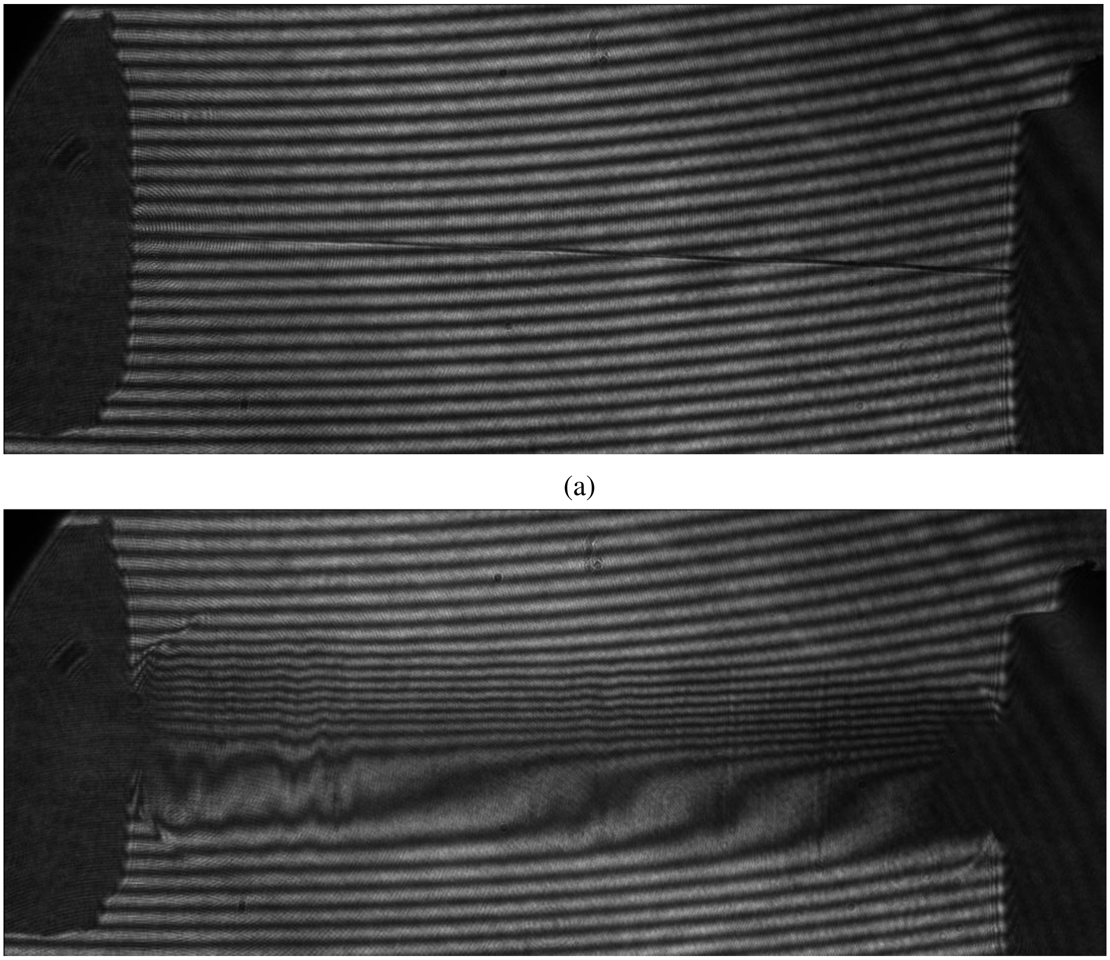
(a)

(b)

Figure 1.1: (a) Interferogram at 532 nm of a single Al wire pre-shot. (b) Interferogram at 532 nm of a single Al wire at 200 ns.

An example of two separate interferograms is provided in Fig. 1.1. The first image was taken before the wire was ablated by a pulsed power source. This image is used as a reference when post processing. The second image was taken at 200 ns after wire ablation. Note how the fringes are shifted during wire ablation process. The process of evaluating the fringe shift will be explained in Chapter 3.

The engineering challenge for this setup is to create the optical experiment. Any time an optical experiment is setup, there is a significant effort involved in planning, design, installation, alignment, and focusing of optics. Without proper care during this step, results obtained may be inaccurate or difficult to analyze.

There are many published and accepted methods to perform an interferometry experiment [1, 11, 12]. We plan to evaluate some of the methods and choose the most effective method for our work.

1.3 Research Hypothesis

We aim to improve upon the state of the art in diagnostics for plasma parameter measurement through further development of dual-wavelength interferometry. This will yield measurement results of electron density, atomic density and expansion velocity after wire ablation from a pulsed power source. Specifically, we intend to estimate electron and atomic densities, determine plasma conditions and determine the accuracy of the method.

1.4 Outline

Here, we explain the organization of the remainder of the thesis document. In Chapter 2, we will provide references to the current state of the art in experimental diagnostics and experimental plasma creation. These previous works lay the foundation for our work and provide opportunities for advancement of the technology. In Chapter 3, we will describe in great detail the technique of interferometry. Starting with single-wavelength interferometry, we progress into dual-wavelength interferometric analysis, and present plasma parameter estimates. Chapter 4 will contain results for different materials. Chapter 5 summarizes our work.

Background

2.1 Previous Work

A survey of plasma physics experiments focused on techniques using pulsed power as an energy source in the generation of plasma [1, 11, 12]. The review of optical techniques considered interferometric experimental setups and basic optical techniques [1, 11, 12].

Experiments by Sarkisov et al. [1] used a pulsed power technique to perform wire ablation along with several optical and electrical diagnostics to measure the plasma parameters. Samples consisted of single metallic wires between 10–38 μm in diameter and 20 mm in length installed into a vacuum chamber at mTorr pressure. These wires were ablated by the pulsed power source which delivered a maximum current rate of 150 A ns^{-1}. Electrical diagnostics were employed to measure current with a shunt resistor and voltage measured with a capacitive divider. The authors' goal was to evaluate the initial stage of wire ablation, a necessary understanding for fusion research. They used single wavelength interferometry, shadowography and emission spectroscopy to analyze atomic density, temperature, expansion velocity and how the sample is affected throughout the current pulse.

While discussing the interferometry technique, Sarkisov proposed Eq. (1.1) which relates fringe shift δ to atomic polarization α, atomic density N_a and electron density N_e. Phase shift and its correlation to fringe lines and interferometry will be further explained in Chapter 3. The coordinates in Eq. (1.1), x, y are defined where x is in the direction of the propagation of the probing laser and y is normal to the wire axis and probing direction [1].

Equation (1.1) cannot be solved directly. Sarkisov stated that there are three cases in which one can reconstruct electron and/or atomic densities through this density equation. In a high temperature plasma (10–100's eV), the electron densities are significantly greater than atomic densities. Thus, the contribution from the neutral densities is negligible and the equation can be simplified. The electron density could be recovered with single wavelength interferometry. In the second case, we consider low temperature plasma. In this case, the atomic densities are much greater than the electron densities and the equation can again be simplified and atomic densities resolved with single wavelength interferometry. In the final case, electron and atomic densities are comparable and two-wavelength interferometry is necessary to resolve each value [1].

After explanation of experimental setup and some theory behind the work, Sarkisov began analysis of the diagnostics to determine the plasma parameters. Through interferometry he found the gaseous atomic density, N_a, to be on the order of 4.3×10^{19} cm^{-3}. Shadowgrams taken using the shadowography technique, show that the expansion velocity of plasma through his wire ablation experiment was on the order of 3.5 km s^{-1}. Emission Spectroscopy was used to estimate the temperature of the plasma at 4–6 eV. Though, only single-wavelength interferometry was performed in his work, it was later mentioned that he intended to publish two-wavelength interferometry in a future paper [1]. After contacting him, he mentioned he has not yet published on dual-wavelength interferometry.

There were two publications in 2016 [11, 12] that utilized dual-wavelength interferometry to determine densities in laboratory plasma. Both publications generated plasma using dissimilar techniques and achieved noticeably different results in densities. This difference is due to the methods used to generate the plasma.

Wu et al. [11], concentrated on the energy deposition and vaporization of metallic wires. In this work, 15 μm Al or W wires were placed in a parallel configuration into a vacuum chamber with a pulsed power source. The vacuum removed other impurities from the experiment to simplify results. Temporal and spatial comparisons were made between aluminum and tungsten wire ablations. The comparisons included expansion velocity and surface densities. In Wu's experiment, the pulsed power source delivered 100 A ns^{-1} to both wires. Dual-wavelength interferometry was used to measure atomic and electron densities. Current and voltage were measured with a Rogowski coil and a resistive voltage divider respectively. Optical emission was measured with a photo tube for temperature measurements. The probing laser produced the first and second harmonic at 532 nm and 1064 nm with a pulse width of 30 ps.

The density model of [11] is slightly different from Eq. (1.1). Instead of a numerical coefficient in front of the electron density term, Wu defines this to be the classical electron radius. Wu et al. observed the expansion velocity of Al wires was 7.3 km s^{-1}, while W wires were 3.7 km s^{-1}. Since there were two parallel wires, an interesting portion of his work was the merging of the plasma between the wires. Densities of this central region and near the wires were observed. Wu defines these densities as surface densities and represented in units of cm^{-2}. Measured data showed the electron densities to be almost negligible as the current applied was just enough to vaporize the wires with little ionization. Maximum surface atomic density, mass per unit area integrated along the laser path, was $2.2{\times}10^{18}$ cm^{-2} at 53 ns after initial current pulsed the wires. At 336 ns most of the mass merged into the center region defined as the stagnation region. Here, the surface atomic density is $1.6{\times}10^{18}$ cm^{-2} [11].

The specific interferometry technique used for measurement was not mentioned in [11], and the fringe lines were manually traced to measure fringe shifts. The measured fringe shift distances were input into a MATLAB algorithm to determine the specific density information presented in [11].

Yang et al. [12] describes a different way to generate plasma and use dual-wavelength interferometry to discern the atomic and electron densities. In his method, a high-power-density laser heats up a small area of a Cu sample. This heating creates plasma that expands away from the sample into air. This method of creating plasma is known as laser induced plasma (LIP) [12].

The Cu plasma was created with a 20-ns pulse from a neodymium-doped yttrium aluminum garnet (ND:YAG) laser [14] at 1064 nm and 24 mJ [12]. A plano-convex lens was used to focus this beam. The optical experiment, used to measure plasma parameters, employed a Mach-Zehnder [15] interferometry technique. A separate probing laser was used to conduct the interferometry measurement with wavelengths of 1064 nm and 532 nm. The pulse width of this probing laser was not defined. To conduct the Mach-Zehnder interferometry experiment, the probing laser underwent an amplitude division and took separate but equal path lengths until recombined. One of the paths was routed through the Cu plasma, while the other path traversed free space. After recombining, the beam then underwent wavelength division through the use of a dichroic mirror [16] and both interferometric images were collected with separate charge-coupled devices (CCDs) [17].

Yang found that the dual-wavelength interferometry technique was not well-suited for this study as not only were Cu atoms and free electrons present, but also interference due to air, as the measurement is conducted at atmosphere. In fact, he mentioned that three-wavelength interferometry would be better suited for this experiment. To simplify his study, he created two assumptions that allowed for atomic and electron density measurements. First, Yang assumed the plasma core occurs very near the heated surface. In the core, only Cu atoms, free electrons and Cu ions exist. He later showed analysis of interferometry images where he defined this region. The second assumption was that the atomic polarizability of Cu was significantly greater than air. This assumption means that the contributions to fringe shifts are dominated by the Cu particles. These two assumptions allowed progress to be made on the experiment.

Yang analyzed the interferograms using a Delauney triangulation algorithm and Abel transformation [12]. He showed that the atomic density in the core region was 4.6×10^{24} m^{-3}, and the electron density was 1.1×10^{24} m^{-3}. Temperature of the plasma was not measured in this experiment.

2.2 Technical Component

In Section 2.1, we identified the current state-of-the-art in laboratory diagnostics to show how two separate wavelengths were used to evaluate plasma expansion velocity, electron densities and atomic densities with dual-wavelength interferometry. Both wire ablation and LIP techniques were used to generate the plasmas. These plasma generation techniques are very complicated areas of study in themselves.

In the wire ablation technique, a pulsed current is applied to the wires. The wires undergo several changes of state. The wires melt into a liquid before expanding into a gas cloud. If enough energy is remaining, the gas cloud of the metal begins to ionize. These cold plasmas described above with the wire ablation technique are primarily dominated by atomic particles and electron densities are difficult to extract.

The other technique discussed was LIP. In this technique, a 1064 nm, 20 ns laser pulse heats a metallic sample until plasma forms. In this method, electron densities are comparable to the atomic densities in the core region. It is apparent that two-wavelength interferometry was well-suited for measurement of densities in the core region when considering the assumptions that were made. Additionally, these interferometric observations utilize different methods to solve for the densities.

In [1], the electron densities were negligible and simplified the solution from Eq. (1.1). The fringes from single-wavelength interferometry were manually measured and codes were developed to solve for N_a and N_e utilizing the measured phase shift. Wu used a very similar computation for atomic densities even though dual-wavelength interferometry was employed [11]. Yang [12] utilized dual-wavelength interferometry to generate results for both atomic and electron densities. Yet, [12] was the only report successful in estimation of atomic and electron densities using dual wavelength interferometry. Certainly, the computation of densities is the most critical part of this work.

2.3 Technical Challenges

As mentioned in Chapter 1 and observed in Section 2.1, electro-optical techniques are employed to observe densities with dual-wavelength interferometry. Any time an optical experiment is utilized, the design, installation, alignment and focus of the experiment are not trivial. Secondly, analysis of the interferometry images is challenging because of the time variation.

There are still many areas of this work that need to be resolved. It is evident that Yang was successful with the measurement of both densities. This is attributed to comments made by Sarkisov [1] that the electron and atomic densities must be comparable. In [1, 11], the authors negate the contributions from electron density to enable computation of atomic densities. One thing that is not clear to us is when it is acceptable to negate the contribution from one density or the other. Perhaps it is possible to modify the experiment and create ideal conditions for when this could be realized. Lastly, there was no mention in any of these publications to assign a percentage of error in the calculations. It would be useful to know the precision of a dual-wavelength interferometry measurement.

2.4 Summary

In this chapter, we reviewed several publications that set the stage for our study. Sarkisov utilized a pulsed power technique to ablate individual metal wires [1]. The source delivered 150 A ns^{-1} to ablate the wires. Unfortunately, he did not see enough electron density, so only atomic density results were provided. He was the first to model density as a function of phase shift, but the equation that cannot be solved directly for electron and atomic densities. Wu, utilized a similar, but dual-wire technique. In this case, only 100 A ns^{-1} was delivered to the pair of wires in parallel to the source [11]. Again, no discernible electron density could be measured. The density model was simplified to reach a solution for atomic density. Lastly, Yang used LIP to generate the plasma. He was able to solve for both atomic and electron densities using an Abel transform technique [12]. We will thus try to build upon this interferometric work with wire ablation and LIP and show how dual-wavelength interferometry can be a diagnostic for the plasmas created in our laboratory.

Methodology

3.1 Proposed Study

We set out to measure both atomic and electron density using a dual-wavelength interferometry method. For this method, we utilize the first and second harmonic from an ND:YAG laser [14], routed through optics and the plasma chamber, to create interferograms for each wavelength. The fringe shifts in the plasma region of the interferograms are measured, and estimates of atomic and electron densities are calculated. The underlying assumptions, experimental methods, and mathematical approach are further detailed in this chapter.

3.1.1 Experimental Setup

Experiments were conducted at the Antenna and Electromagnetic Technology Branch (RYMH), Plasma Physics and Sensors Laboratory (PPSL), located at the Sensor's Directorate on Wright Patterson Air Force Base. In the PPSL, a section of the laboratory is dedicated to pulsed power research. In this area, an 8 ft $\times$ 4 ft optics table supports the plasma chamber, optical setup and measurement equipment.

The plasma chamber has an experimental volume of 10 cm^3. The configuration of the chamber is 6 sided with 15.24 cm flanges on each side. The top flange is utilized for mounting the electrode configuration and feed through of the high Voltage pulsed-power cable. The bottom flange is connected to a vacuum pump, capable of creating a vacuum

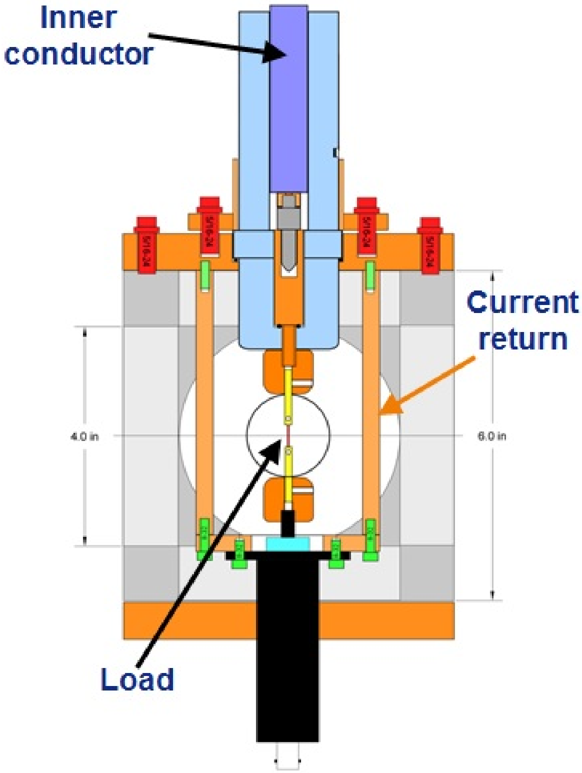

Figure 3.1: Illustration of plasma chamber and electrode configuration.

of sub-mTorr pressure.. The side flanges are fitted with optically transparent windows to allow for optical diagnostics. Figure 3.1 shows a drawing of the electrode configuration. The vacuum chamber is mounted on a non-conductive slab to insulate from the electrically noisy, grounded table. The anode of the electrode assembly is connected to the center conductor of the high voltage cable. The anode connection is insulated from electrical contact with the chamber. The cathode outputs through a current viewing resistor (CVR) of $0.05\ \Omega$ in parallel configuration with the return path through the chamber to the pulsed-power source along the shield of the high voltage cable. A thin, metallic wire is placed in the chamber between the electrodes and serves as the load.

The pulsed-power unit is manufactured by FID GmbH [18]. This unit was specifically designed for PPSL and provides 80 kV, 2.5 kA with a rise time of 10 ns. These specifications are equivalent to 0.2 J of energy. A high-voltage cable is connected from the pulser to the plasma chamber.

The probing laser used for this experiment is a New Wave (Tempest 10) ND:YAG laser [19]. The fundamental wavelength is 1064 nm and the beam propagates through a frequency doubling crystal to obtain the second harmonic of 532 nm. Both wavelengths are contained in a single pulse of the probing laser. The pulse length of the laser is 10 ns with energy output of 100 mJ. There are separate trigger inputs for the flash lamp and Q-switch.

Cameras used to collect the optical information are FLI Microline series CCDs with an ML 8300 sensor [20]. These CCDs provide a resolution of 3326 × 2504 pixels. This provides high resolution images for accurate analysis of the interferograms. Exposure time is set to 100 ms. The CCDs are ideal for this experiment as they can be configured to operate from the leading edge of a trigger input.

The laser, pulser and CCDs are connected to a Berkeley Nucleonics Corporation (BNC) (Model # 575) 4-channel signal delay generator [21]. The purpose of the signal delay generator is to transmit a trigger signal to each device at a prescribed time. The sequence begins through a manual push of the trigger button or a command through USB input. Each connection can be configured to delay the trigger signal or wait until the initialization of a separate channel. Configuration of channels that trigger upon the button push require a synchronization setting of T_0. Table 3.1 shows the configuration of the signal delay generator.

Table 3.1: SIGNAL DELAY GENERATOR CONFIGURATION

Device	Connection	Sync	Width (s)	Delay (s)
CCDs	A	T_0	0.002	0.000000000
Pulsed Power Source	B	T_0	0.002	0.020000000
Laser Flash Lamp	C	T_0	0.002	0.019760140
Laser Trigger	D	C	0.002	0.000240000

An HP Infinium (model# 54845A) oscilloscope [22] is used to measure voltage across the CVR and voltage from the diagnostic probe at the anode. It then becomes necessary to design the optical configuration used to conduct the interferometric measurement. Figure

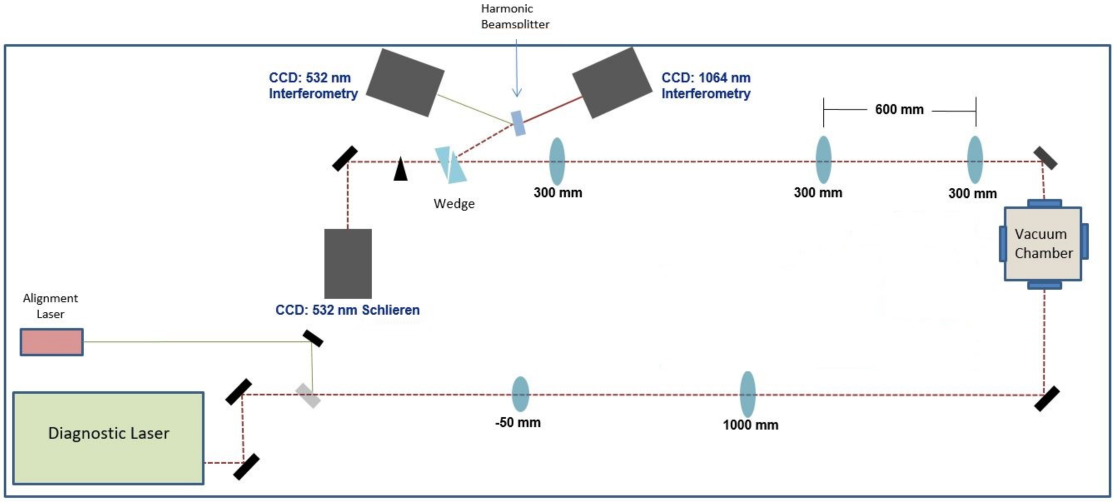

Figure 3.2: Experimental layout used in PPSL.

3.2 shows a picture of this experimental layout.

To begin the installation of this setup it is helpful to use an alignment laser, and additionally for later modifications and adjustments. Here, the alignment laser is 532 nm and continuous wave. This laser is used to define the optical path and for placement of optics. Once completed, the diagnostic probing laser is aligned to share the same optical path. The diagnostic laser is routed through several optics. First, the laser passes through a negative 50-mm focal length lens for beam expansion. Then, a 1000-mm focal length lens is placed in line with the beam path to set the beam waist to be large enough to fill the window of the plasma vacuum chamber. This beam passes through the region of the chamber in which the wire sample is placed. This volume of the test region is referred to as the object. After passing through the object, the beam is then routed through a relay system. Here two 300-mm focal length lenses are positioned at a 600-mm distance to extend the image of the object. An exact copy of the image incident upon the first lens is transmitted through the second lens. The beam is then guided through a third 300-mm focal length lens and positioned to provide adequate magnification on the CCDs. The beam is then incident upon an air-wedge shearing interferometer and reflected back towards the CCDs. This type of interferometer will be further explained later in the next section. Before entering the CCDs, a harmonic beam splitter is used for wavelength division to separate the 532 and 1064 nm wavelengths.

Each time an experiment is conducted, a wire sample is loaded in between the electrodes. The vacuum chamber is pumped down to less than 10 mTorr. The purpose of the vacuum is to remove impurities present in the air. The experiment is conducted and results in two interferograms. Each interferogram is representative of a specific wavelength taken at a prescribed instance in time during the wire ablation process. A new sample is loaded into the chamber and the experiment is repeated until the entire lifetime of plasma is imaged.

3.1.2 Interferometry

As mentioned during the introduction, interferometric techniques have been used since the 17th century. There are a number of techniques to generate fringe shifts due to the interference of two light sources. Some of the common methods include Michelson, Mach-Zehnder, Sagnac, Twyman-Green, Fabry-Perot and a shearing air wedge interferometer [8]. One thing they all share is a coherent light source. Two light waves are coherent if the difference in phase is constant and each wave is monochromatic. It is well known that that the velocity of light in a vacuum c is 299792458 m s^{-1}. When light waves are traveling through a non-vacuum medium, this velocity υ is changed by a factor of the refractive index η.

$$\upsilon = \frac{c}{\eta} \tag{3.1}$$

The index of refraction for plasma, the medium of interest to us, is defined in (3.2) [23].

$$\eta = \sqrt{1 - \frac{\omega_{pe}^2}{\omega^2}} \tag{3.2}$$

Here, ω_{pe} is the plasma frequency for a collisionless, unmagnetized and cold plasma, and defined in (3.3) [23].

$$\omega_{pe} = \sqrt{\frac{4\pi N_e e^2}{m_e}} \tag{3.3}$$

Here, N_e is electron density in cm^{-3}, e is charge of electron in statcoulombs and m_e is mass of electron in grams. Finally, the index of refraction is proportional to the effective permittivity as defined in (3.4) [23].

$$\epsilon_r = 1 - \frac{4\pi N_e e^2}{m_e \omega^2} = \eta^2 \tag{3.4}$$

In the Michelson and Mach-Zehnder interferometry experiment, which can be used to measure plasma properties, the laser beam undergoes amplitude division into two beams. One beam is routed through a plasma and is considered the probing beam. The second beam is known as the reference beam and does not pass through the plasma. Both beams travel the same path length before recombining. Propagation path differences cause phase differences, which result in interference fringe patterns. In this case, there is not a fringe spacing based upon path length difference as both path lengths are equal. Rather, the different electric permittivities along the path of the probing beam will cause a phase shift that can lead to calculation of atomic and electron densities. Recombining of the beams is not a trivial process.

In the experiments conducted for this report, our monochromatic light source is the diagnostic probing laser. We use an air-wedge shearing interferometer [24] to create the fringe pattern. After the laser beam passes through the plasma, it is incident upon the first lens in the interferometer. A portion of this light is reflected and some transmitted. The transmitted light reflects off the second lens, behind an air gap, and recombines with the first reflection providing an interference pattern. This process causes a phase difference between the two reflections due to the extra distance that the second reflection travels. Since the beam was collimated to a larger area than which plasma existed in the chamber, two regions in the interferogram exist. The first region that surrounds the plasma is considered free

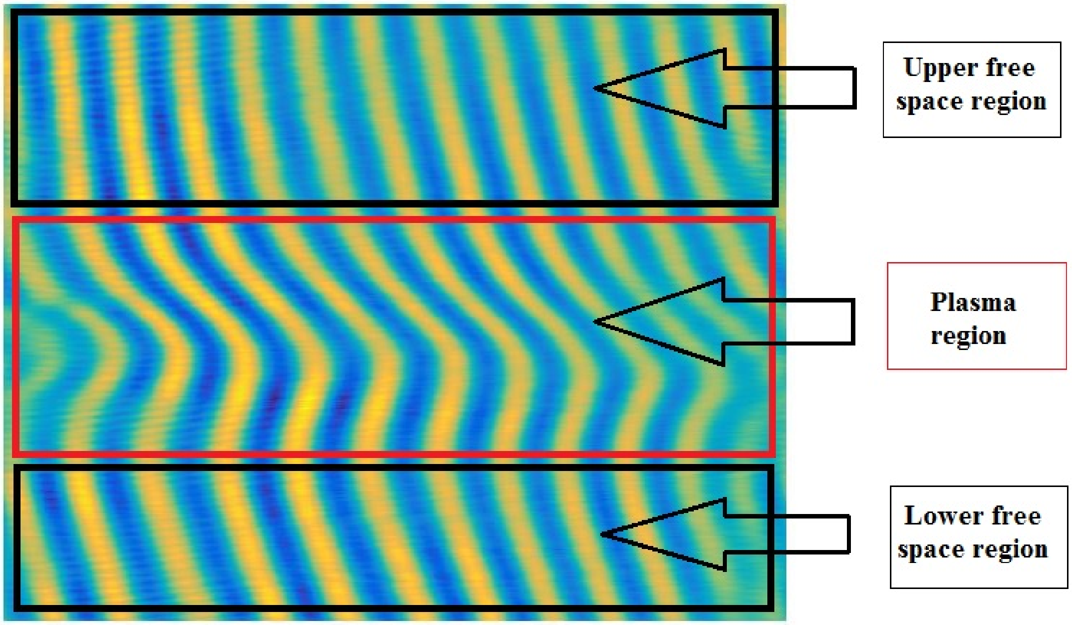

Figure 3.3: Regions of interferogram.

space and the phase difference is due to the path length difference of both reflections. The second region, the plasma region, has phase difference due to the path length difference plus contributions from the atomic and electron densities. This plasma region will create shifted fringes in the interferograms. Due to the arrangement of fringes on the interferograms, we also designate the free space region into upper and lower free space regions. An example is shown in Fig. 3.3.

3.2 Analysis Methods

In this section, we will detail the techniques required to understand how to analyze an interferogram and determine atomic and electron density information. As mentioned previously, fringes are arranged on an image in a periodic configuration. At each wavelength, an image is taken before the shot and at a prescribed time after the current pulse is applied to the wires. The images are time resolved to the pulse width of the probing laser. After literature review, we found that some researchers preferred manually measuring the fringe shifts [11], while others developed or used commercial off-the-shelf programs capable of this task [12] [1]. We use a combination of computer algorithms and manual techniques in order to obtain this information for each interferogram.

In each image collected during the shot, we evaluate three distinct regions. There is an upper free space region that is not perturbed by the plasma, a plasma region that expands radially away from the initial wire position and a lower free space region. We expect that the periodicity of the fringes is unchanged in all three regions. Fringe shift analysis provides the distance fringes are shifted along the plasma region.

The interferograms obtained contains high-frequency noise, DC contributions and poorly defined edges of the fringes. This makes analysis of the images difficult as observed from the line plotted in Fig. 3.4. The DC contribution and noisy edges can be observed through visual inspection. It is necessary to filter the image to allow for proper analysis of the fringes. This is accomplished through applying a window in frequency space. The peaks observed after computing a discrete Fourier transform of the original pixel information are displayed in Fig. 3.5. A window is applied around the positive and negative peaks surrounding the DC contribution. These peaks appear at the periodicity of the fringe lines. All other information is suppressed and the data is transformed back to the, now filtered, spatial domain. The filtered interferogram is presented in Fig. 3.6 and information such as fringe spacing and periodicity is observed without additional contributions from noise and DC.

Additionally, fringe lines in our interferograms are not vertical. The fringes appear with both a curvature and tilt. This is due to the interference pattern created from the air-wedge shearing interferometer. As alignment of the system was ongoing, it was observed that the fringe pattern is a circular configuration with concentric fringe lines emanating away from the center, reminiscent of Newton's rings. It could be desired to find the region in which horizontal fringe lines appear or vertical fringe lines. We chose to use the region

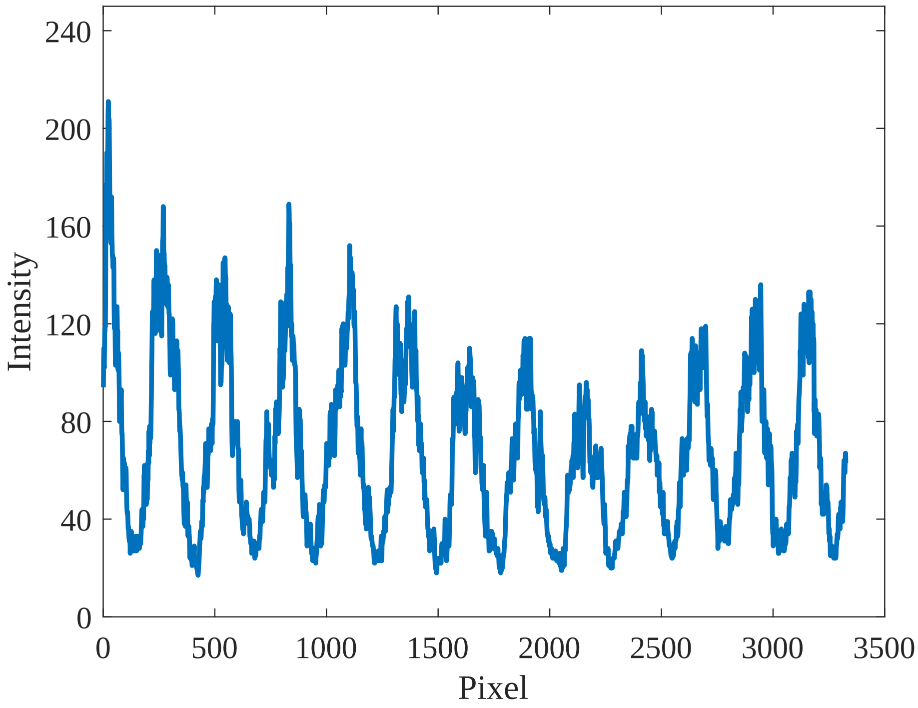

Figure 3.4: Unfiltered row data.

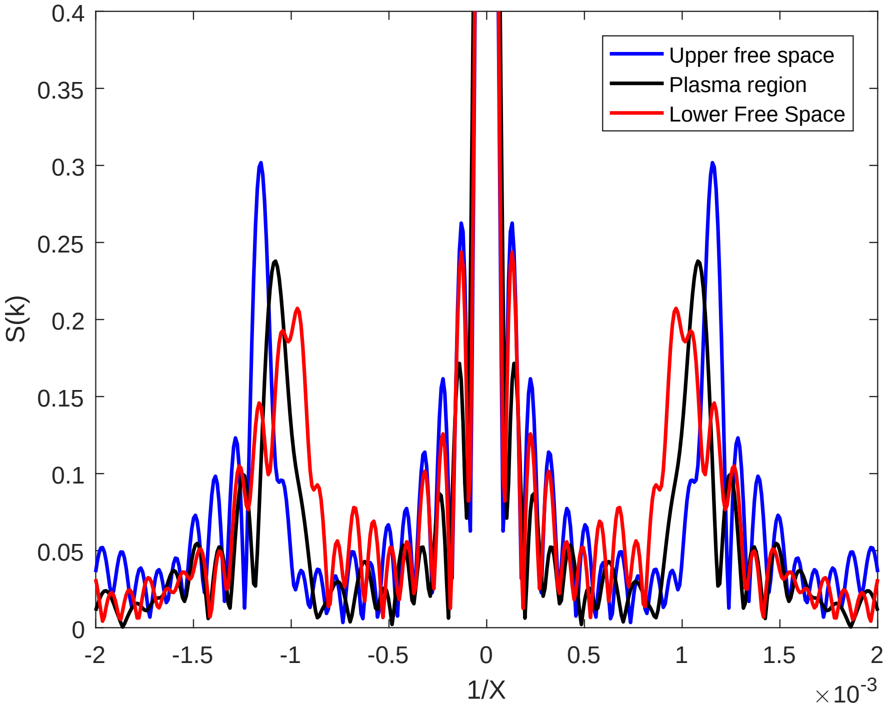

Figure 3.5: Peaks observed after Fourier transform.

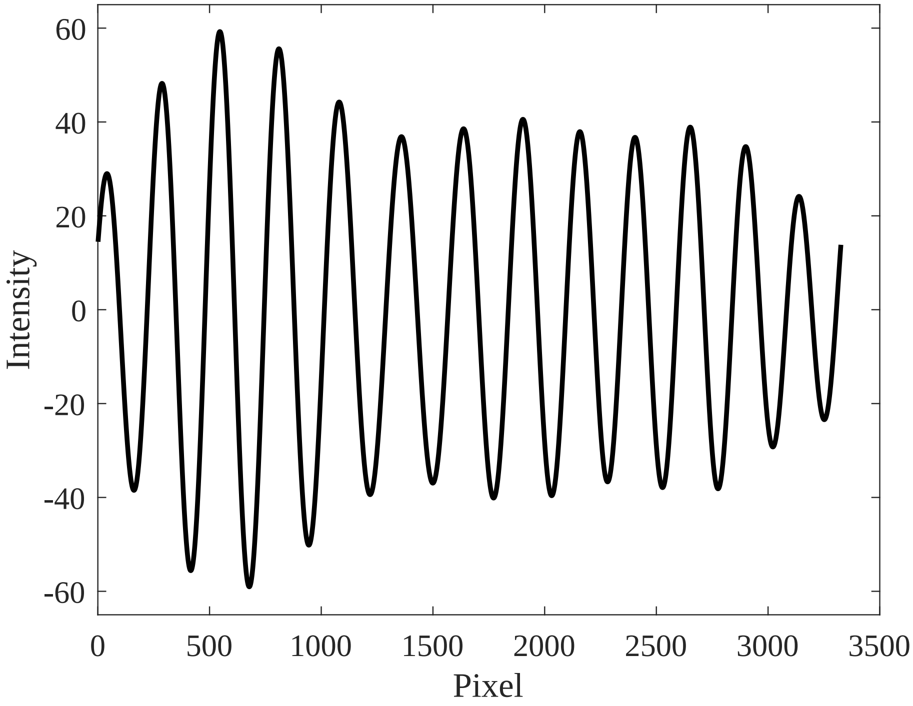

Figure 3.6: Filtered row data.

closest to where vertical fringe lines appeared. This was challenging as adjustments to the air-wedge shearing interferometer affected the 532-nm and 1064-nm images differently. Whether vertical or horizontal, fringe lines are obtained, and the plasma region of the interferogram will shift the fringes proportional to contributions from both atomic and electron density. Our solution to measure the fringe shift from the curved fringes is to create a cubic spline fit from the corresponding free space fringe. The cubic spline fit extends the reference fringe through the plasma region, enabling the fringe shift to be measured. An example of this cubic spline fit is observed in Fig. 3.7 of the filtered data.

Once the fringe shift information has been obtained for each wavelength, we perform analysis of that information. We have utilized a model for fringe spacing from [25].

$$I(x) = I^4 \cos^2 \delta \tag{3.5}$$

Born [25] shows that the intensity model is convenient for relating physical distance

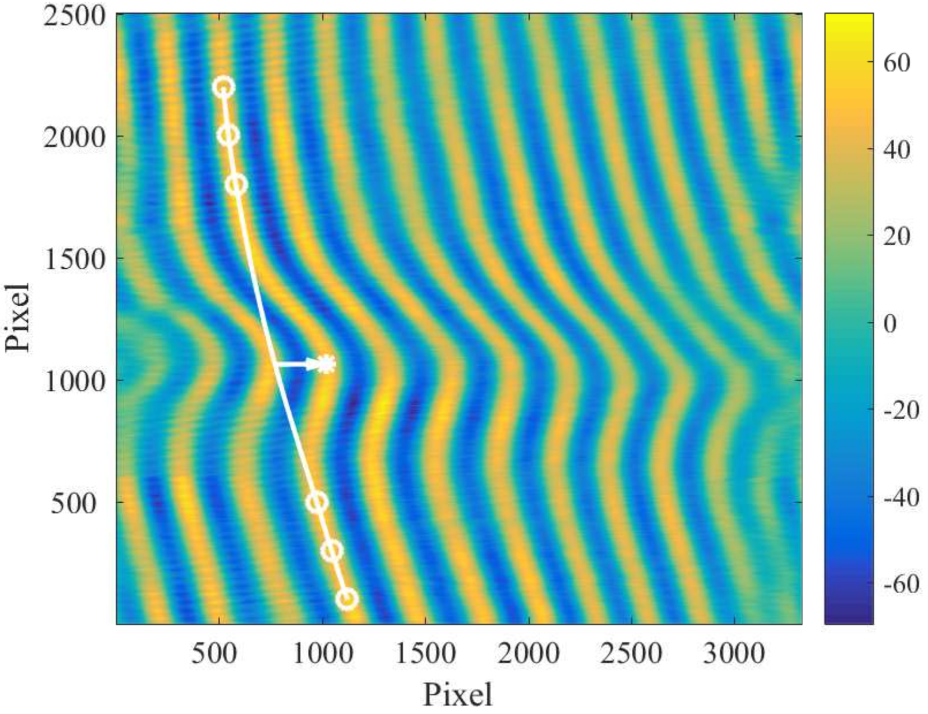

Figure 3.7: Cubic spline fit at 1064 nm.

and wavelength to fringe spacing. This model assumes that both monochromatic sources creating the interference pattern have the same intensity and that the periodicity of the fringe spacing is on the order of π. Each set of dark and light fringes, one complete phase cycle, occurs at multiples of π. Furthermore, Born defines the phase as:

$$\delta_{fs} = \frac{2\pi}{\lambda}\frac{d}{L}x \tag{3.6}$$

Here, λ is the probing laser wavelength in meters, d is the distance between lenses in the interferometer in meters, L is the total distance each source travels from the interferometer to the CCD in meters, and x represents the location being measured in the interferogram. This model works well to analyze fringe spacing.

With a simple model for fringe spacing, we return to the density equation (1.1) for evaluation of both densities. Once the fringe shift information is obtained for 532-nm and 1064-nm interferograms we set up Eq. (1.1) as two equations. We set the first equation variables atomic polarizability α [26] and wavelength λ to represent 1064-nm values, and setting δ equal to the normalized fringe shift observed from the 1064-nm interferogram. In the second equation, we set the variables to represent 532-nm properties and the fringe shift equal to that observed in the 532-nm interferogram. Revisiting Eq. (1.1), we are left with two equations and two unknowns in the densities.

$$\begin{aligned} \delta_{1064} &= \frac{2\pi\alpha_{1064}}{\lambda_{1064}} \int N_a dl - 4.49 \times 10^{-14} \lambda_{1064} \int N_e dl \\ \delta_{532} &= \frac{2\pi\alpha_{532}}{\lambda_{532}} \int N_a dl - 4.49 \times 10^{-14} \lambda_{532} \int N_e dl \end{aligned} \tag{3.7}$$

To enable computation, the line integral for electron density is assigned the variable χ_e. The line integral for atomic density is assigned the variable χ_a, and the two values are determined by solving both equations.

$$\begin{aligned} \delta_{1064} &= \frac{2\pi\alpha_{1064}}{\lambda_{1064}} \chi_a - 4.49 \times 10^{-14} \lambda_{1064} \chi_e \\ \delta_{532} &= \frac{2\pi\alpha_{532}}{\lambda_{532}} \chi_a - 4.49 \times 10^{-14} \lambda_{532} \chi_e \end{aligned} \tag{3.8}$$

3.3 Summary

In this section, we defined the methods used to measure two-wavelength interferometry. The experimental configuration was discussed to describe the plasma chamber, optical configuration and diagnostics. Interferometry techniques were explained. Lastly a brief mention of analytical methods was described with lots of room for improvement.

Experimental Results

In this chapter we will describe the experimental results obtained during this effort. We will first take a look at the conditions observed during the experiment. Then, we will examine the fringe shift measured for each of the experiments. The fringe shift measurements will lead to calculation of the densities as described in Chapter 3. Interferograms collected during this effort are presented in Appendix A and B.

4.1 Experiment Description

Before each experiment is conducted, a new sample is loaded into the vacuum chamber. The top flange is unbolted from the chamber and a 25 μm, 99.99$\%$ purity, copper wire is installed between the electrodes. This is quite challenging as the wires are small and can easily break if not handled carefully. Tweezers and a jewelers hat with a light, makes this part a little easier. The distance between the electrode is 10144.76 μm. The ends of the wires are trimmed away so that they do not interfere with the interferogram. A small piece of heat shrink tubing is placed over each of the electrodes to hold the wire in place. At this time a resistance value is measured between the electrodes. This value can be observed in Table 4.1 for each experiment. A high resistance value at this point is indicative of the wire not making good contact with the electrodes. If a resistance measurement greater than 5 Ω between the electrodes is observed, the sample is removed and a new sample installed. Resistivity of Copper for 100$\%$ purity is 1.7×10^{-8} Ω m. The theoretical calculation of resistance for a similar length of 100% pure copper wire is 0.3513 Ω. This can be found by solving for $R = \frac{\rho l}{A}$. Here, ρ is resistivity, l is the length of the wire and A is the cross sectional area.

After proper installation of the wire sample, the top flange is installed to the chamber. The vacuum pump is activated, and the pressure is lowered to less than 10 mTorr. This pressure, much lower than atmospheric pressure at sea level (760 Torr), removes most of the impurities from the environment that will be probed by the laser. These values are tabulated in Table 4.1 and 4.2.

4.2 Fringe Shift

In this section we present the measured values for the fringe shifts. Interferograms were collected at 532 nm and 1064 nm. Fringe spacing, measured in free space, was defined in Eq. (4.1).

$$\begin{gathered} \delta^{(fs)}_{1064nm}[\text{pixels}] \\ \delta^{(fs)}_{532nm}[\text{pixels}] \end{gathered} \tag{4.1}$$

As described in Section 3.2 a cubic spline fit was applied to the reference fringe line and the distance measured between this cubic spline and the maximum point of fringe shift was measured in pixels.

$$\begin{gathered} \delta^{(p)}_{1064nm}[\text{pixels}] \\ \delta^{(p)}_{532nm}[\text{pixels}] \end{gathered} \tag{4.2}$$

The normalized fringe shift value δ, as defined in Eq. (3.8), was calculated as a ratio of fringe shift vs. fringe spacing, and resulted in units of fringes. These values were

Table 4.1: PARAMETERS OBSERVED DURING COPPER EXPERIMENTS

Experiment	Time (ns)	Resistance (Ω)	Pressure (mTorr)	δ_{1064} fringes	δ_{532} fringes	N_e cm^{-3}	N_a cm^{-3}
1	0	3.7	8	0	0.000	NAN	NAN
2	50	2.8	9	NAN	NAN	NAN	NAN
3	100	1.3	8	NAN	NAN	NAN	NAN
4	150	1.7	8	3.399	NAN	NAN	NAN
5	200	1.2	8	2.348	NAN	NAN	NAN
6	250	2.6	9	1.888	NAN	NAN	NAN
7	300	2.7	8	1.518	3.212	1.76×10^{18}	4.31×10^{19}
8	350	2.7	9	1.105	2.583	6.44×10^{17}	3.02×10^{19}
9	400	2.7	9	0.956	2.318	4.34×10^{17}	2.60×10^{19}
10	450	2.2	9	0.954	2.112	5.33×10^{17}	2.01×10^{19}
11	500	1.6	8	0.632	1.586	1.70×10^{17}	1.36×10^{19}
12	550	1.5	8	0.617	1.246	4.36×10^{17}	1.02×10^{19}
13	600	2.1	8	0.570	1.112	1.90×10^{17}	9.65×10^{18}
14	150_1	1.1	8	3.177	NAN	NAN	NAN
15	150_2	2.4	8	3.118	NAN	NAN	NAN
16	150_3	1.6	5	2.888	NAN	NAN	NAN
17	150_4	1.6	8	3.110	NAN	NAN	NAN
18	150_5	2.6	8	2.826	NAN	NAN	NAN
19	150_6	2.6	6	3.095	NAN	NAN	NAN
20	300_1	1.9	5	1.431	2.856	1.77×10^{18}	3.94×10^{19}
21	300_2	1.6	6	1.588	3.271	1.81×10^{18}	4.56×10^{19}
22	300_3	1.2	7	1.424	3.008	1.51×10^{18}	4.23×10^{19}
23	300_4	1.3	8	1.591	3.270	1.82×10^{18}	4.56×10^{19}
24	300_5	2.8	8	1.537	2.957	2.07×10^{18}	4.03×10^{19}
25	300_6	1.7	8	1.500	NAN	NAN	NAN
26	450_1	1.3	8	1.020	2.153	6.06×10^{17}	2.11×10^{19}
27	450_2	3.1	8	0.751	1.891	7.58×10^{17}	1.95×10^{19}
28	450_3	1.8	8	0.849	2.109	2.37×10^{17}	2.17×10^{19}
29	450_4	1.2	8	0.977	1.779	2.98×10^{17}	1.66×10^{19}
30	450_5	1.4	9	0.866	1.866	6.03×10^{17}	1.84×10^{19}
31	450_6	1.5	7	0.842	2.171	2.12×10^{17}	2.25×10^{19}
32	600_1	3.2	9	0.535	1.072	3.77×10^{17}	8.52×10^{18}
33	600_2	1.3	9	0.413	1.063	8.73×10^{16}	9.07×10^{18}
34	600_3	3.0	5	0.417	1.120	4.78×10^{16}	9.64×10^{18}
35	600_4	2.8	6	0.496	1.293	9.07×10^{16}	1.10×10^{19}
36	600_5	3.0	7	0.508	1.234	1.71×10^{17}	1.04×10^{19}
37	600_6	1.3	9	0.478	1.200	1.27×10^{17}	1.02×10^{19}

Table 4.2: PARAMETERS OBSERVED DURING ALUMINUM EXPERIMENTS

Experiment	Time (ns)	Resistance (Ω)	Pressure (mTorr)	δ_{1064} fringes	δ_{532} fringes	N_e cm^{-3}	N_a cm^{-3}
1	150	1.2	9	2.09	4.07	2.51×10^{18}	6.15×10^{19}
2	300	1.2	8	0.594	1.41	7.06×10^{16}	1.08×10^{19}
3	450	1.1	9	0.316	0.87	7.60×10^{16}	6.08×10^{18}
4	150_1	3	3	1.61	3.65	5.32×10^{17}	4.19×10^{19}
5	150_2	1.8	9	2.04	3.43	3.22×10^{18}	4.40×10^{19}
6	300_1	1.7	9	0.74	1.73	1.26×10^{17}	1.49×10^{19}
7	300_2	1.7	9	0.70	1.54	2.19×10^{17}	1.21×10^{19}
8	450_1	1.2	9	0.47	1.17	1.42×10^{16}	7.98×10^{18}
9	450_2	1.5	8	0.39	0.97	6.30×10^{15}	6.82×10^{18}

determined from copper and aluminum samples, and summarized in Fig. 4.1.

$$\begin{aligned} \delta_{1064} &= \frac{\delta_{1064}^{(p)}}{\delta_{1064}^{(fs)}} \\ \delta_{532} &= \frac{\delta_{532}^{(p)}}{\delta_{532}^{(fs)}} \end{aligned} \tag{4.3}$$

During evaluation of the fringe shifts, several observations were made. The plasma region of images collected before 150 ns were indecipherable. The probing laser was unable to propagate through this region and fringe shifts could not be observed. Therefore, our observations were made from 150 to 600 ns. The plasma region for images collected at 532 nm was unobservable before 300 ns for copper samples. Fringe shifts for the 532 nm plasma region were observed from 300 to 600 ns. Fringe Shifts could be observed for copper samples at 1064 nm from 150 ns to 600 ns. Additionally, aluminum fringe shifts were observed at both wavelengths from 150 ns to 450 ns. In both cases, measurements were collected every 50 ns up to 1200 ns when the fringe lines returned to the vacuum pattern. The fringe shifts observed in the plasma region from 600 to 1200 ns at both wavelengths were negligible for copper samples and after 450 ns for aluminum samples.

In Fig. 4.1, it is observed that the fringe shift tends towards zero as the plasma dissi-

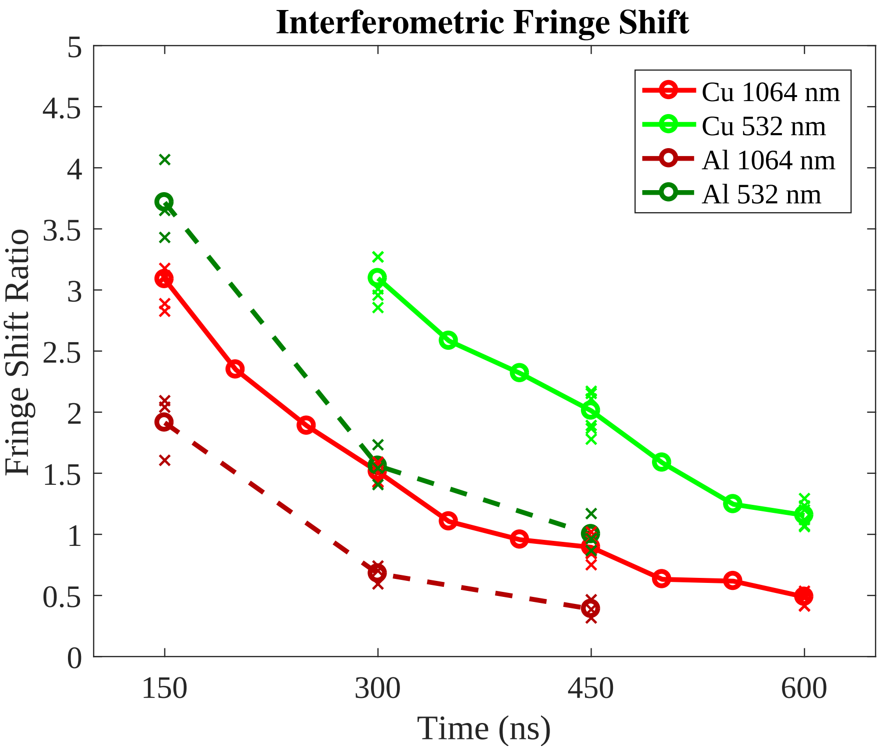

Figure 4.1: Measured fringe shift.

pates. Images for copper samples at 1064 nm show a maximum fringe shift of 3.4 fringes at 150 ns, and a minimum fringe shift of 0.57 fringes at 600 ns. Images for copper samples at 532 nm show a maximum fringe shift of 3.2 fringes at 300 ns, and a minimum fringe shift of 1.1 fringes at 600 ns. Measurements of aluminum samples at 1064 nm include a maximum fringe shift of 2.1 fringes and a minimum of 0.3 fringes. Aluminum wires at 532 nm have a maximum fringe shift of 4.1 fringes and a minimum of 0.9 fringes. The fringe shift is due to the refractive index of electrons and the metallic gas formed during wire ablation. This value decreases over time due to the radial expansion of these parameters away from the center of the wire.

We conducted extra experiments at 150, 300, 450 and 600 ns. At each time step an additional six experiments were conducted to show the repeatability of the experiments as a new sample was used each time. Here, the difference between maximum and minimum of the total fringe shift was computed and displayed with markers. The maximum difference found was 0.7 fringe shifts and the minimum difference was 0.3 fringe shifts. Comparison of error vs. wavelength shows no correlation.

The most intriguing result from fringe shift analysis is the lack of fringe appearance in the plasma region of copper samples collected from 532 nm interferograms before 300 ns. This indicates that the electromagnetic waves transmitted from the probing laser were attenuated and could not pass through this region. These observations were apparent for copper samples, but not for aluminum. I attribute this to the density difference between the samples. Copper has a density of 8.96 g cm^{-3}, while aluminum density is 2.69 g cm^{-3} [27]. The density in copper is almost three times greater than that of aluminum and is a plausible explanation for this observation. Additionally, laser energy measured 1 foot from laser output was 94 mJ at 1064 nm and 21 mJ at 532 nm. This difference in combination with the higher density of copper leads to the missing fringe lines in copper measurements at 532 nm before 300 ns.

Table 4.3: CONFIDENCE INTERVAL FOR COPPER EXPERIMENTS

Time (ns)	$\chi_{\mathrm{L}_{1064\ \mathrm{nm}}}$	$\chi_{\mathrm{U}_{1064\ \mathrm{nm}}}$	$\chi_{\mathrm{L}_{532\ \mathrm{nm}}}$	$\chi_{\mathrm{U}_{532\ \mathrm{nm}}}$
300	1.34	1.69	2.65	3.53
450	0.67	1.12	1.62	2.41
600	0.35	0.63	0.50	1.81

Utilizing the student T-test, we evaluated the copper experiments at the repeated increments of time (300 ns, 450 ns, 600ns) to determine the confidence interval $[\chi_{\mathrm{L}},\ \chi_{\mathrm{U}}]$ for fringe shift measurements. A t-value of 2.447 was selected from the t-table [28]. At the 5% error, with 6 degrees of freedom, the population mean for fringe shift is not in the confidence intervals represented in Table 4.3, with a 5% likelihood.

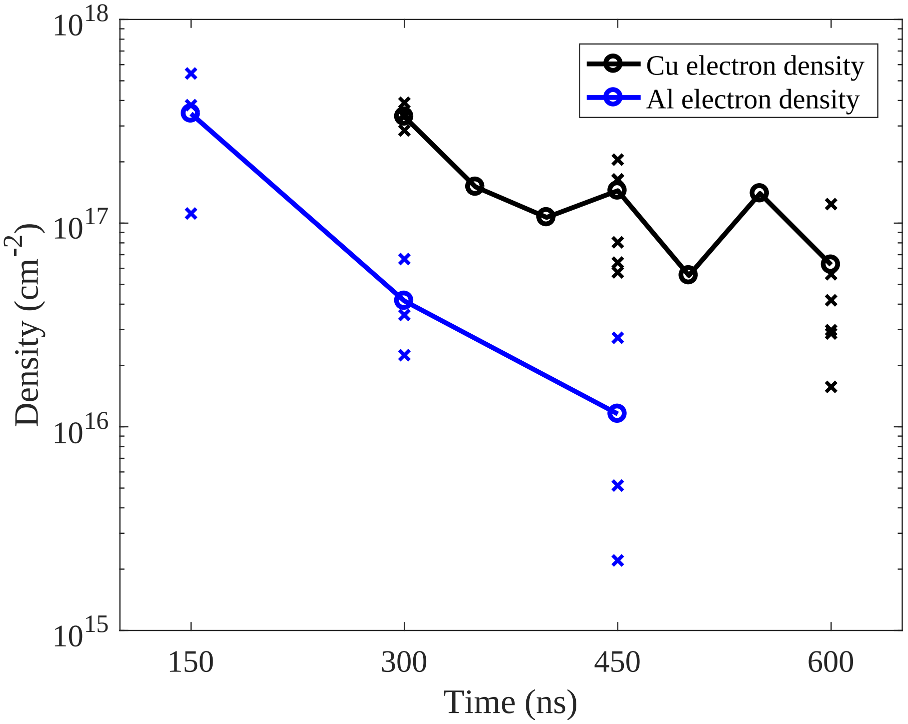

Figure 4.2: Electron effective surface density as calculated from Eq. 3.8.

4.3 Electron and atomic density estimation

In this section, we discuss the electron and atomic densities. After solving Eq. (3.8), as defined in Section 3.2, we display the experimental results in Table 4.1 and 4.2. The results are plotted in Fig. 4.2, 4.3, 4.4 and 4.5. Electron densities are displayed with the y-axis in a logarithmic scale, as the densities range two orders of magnitude. Atomic densities are presented in a linear scale.

Maximum electron effective surface density is 3.44×10^{17} cm^{-2} for copper samples, and the maximum electron efective surface density is 3.8×10^{17} cm^{-2} for aluminum samples. Figure 4.2 shows these densities decreasing as time elapses. This is congruent with what is expected as the measurement we are conducting is at the center of the wire. As the experiment develops, the wire melts, turns into a metallic vapor and begins to ionize. As this process evolves, gas and plasma expand radially away from the initial wire position.

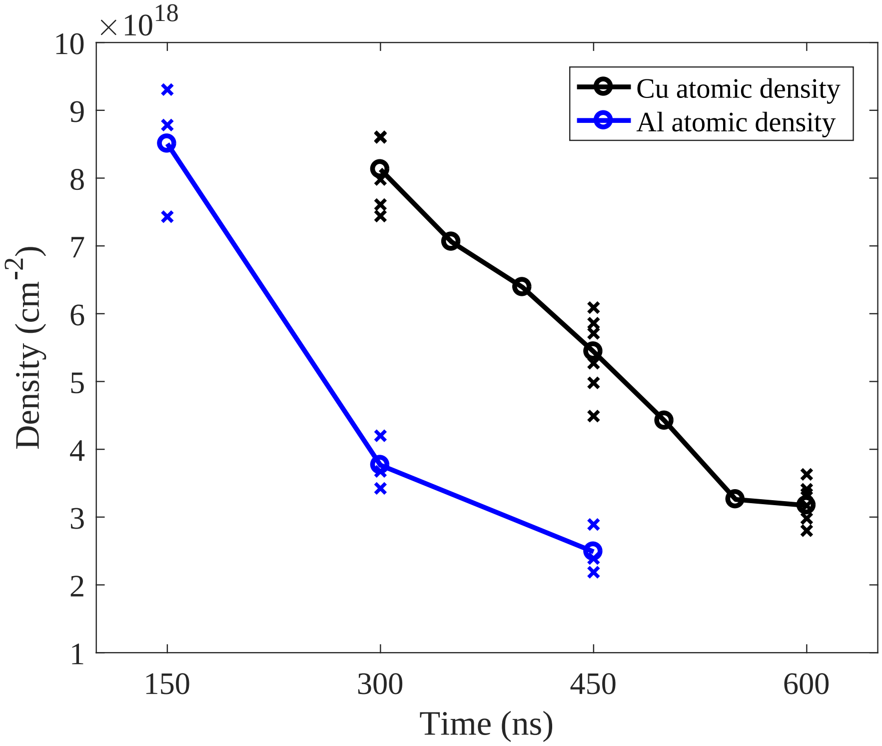

Figure 4.3: Atomic effective surface density as calculated from Eq. 3.8.

A decrease in both densities is therefore expected and observed. In Fig. 4.3, displayed in a linear plot, show that maximum atomic effective surface density is 8.61×10^{18} cm^{-2} for copper samples, and 9.31×10^{18} cm^{-2} for aluminum samples. The atomic density profile also decreases with time.

The additional experiments conducted to represent the repeatability of our work are significant when describing densities. The maximum difference observed for electron effective surface density is 5×10^{17} cm^{-2} for copper samples. These values are substantial and indicate errors in measurement or sample. The maximum difference observed for atomic effective surface density is 4.3×10^{18} cm^{-2} for copper samples. Again, this indicates a very substantial error, even greater than that observed for electron density.

A first order approximation to the volumetric densities is achieved through additional investigation of the plasma region. Measuring the width of this region, and converting from pixels to centimeters, defines the diameter of the plasma region. It is assumed the geometry here is cylindrical and the plasma is homogeneous in this region. The maximum fringe shift

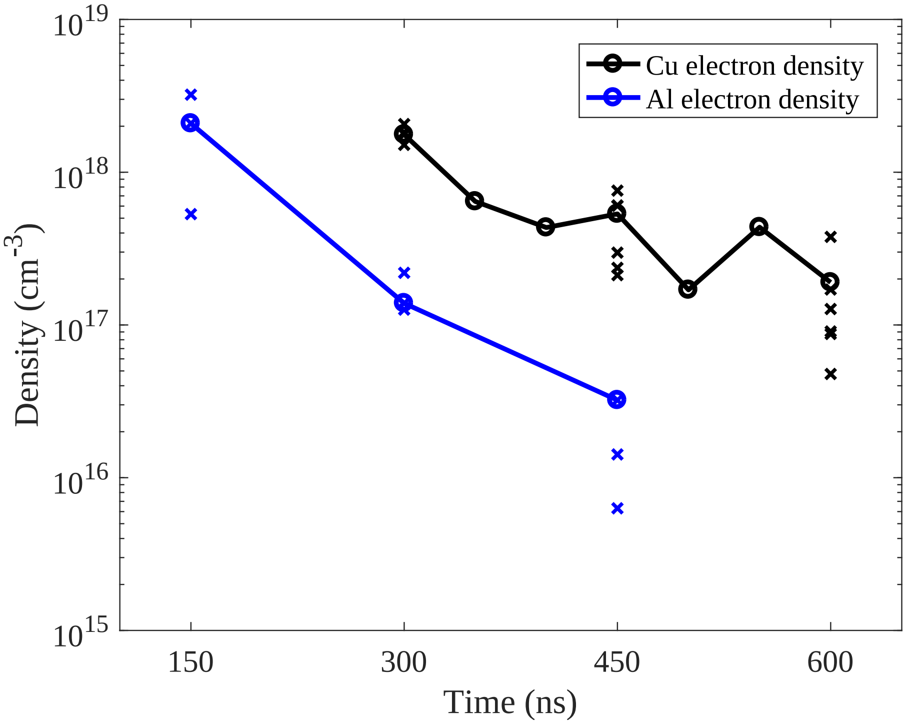

Figure 4.4: Electron density as calculated from Eq. 3.8.

is observed when the laser beam propagated through the entire volume of the plasma, and electron densities were uniform throughout the plasma region. The width of the plasma region increased as time elapsed. At each time increment, the diameter of the plasma cylinders coincide. In order to calculate the volumetric densities, the plasma diameters were divided on the effective surface densities. Results are displayed in Fig. 4.4, 4.5.

The electron density for copper samples show a maximum of $2.07{\times}10^{18}$ cm^{-3}, and $3.22{\times}10^{18}$ cm^{-3} for aluminum. Atomic density results for copper samples show maximum density of $4.56{\times}10^{19}$ cm^{-3}, and $6.15{\times}10^{19}$ cm^{-3} for aluminum. Figures 4.2, and 4.3 provide a more realistic expectation of the atomic and electron densities observed during our experiments.

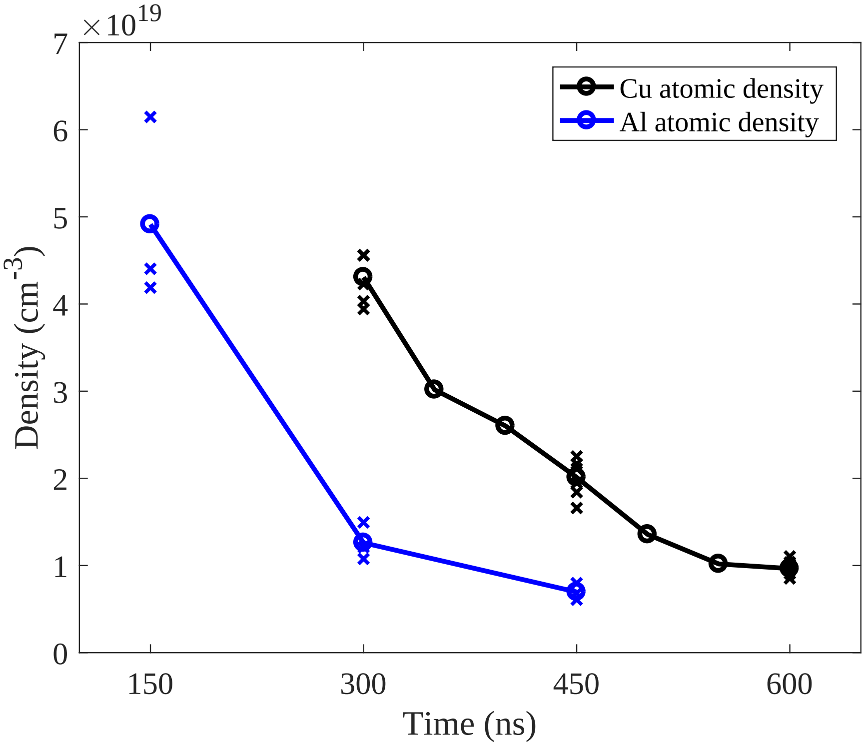

Figure 4.5: Atomic density as calculated from Eq. 3.8.

4.4 Summary

In this chapter we discussed and documented the experimental conditions observed during this effort. We have also presented the measured fringe shift data. The purpose for performing this investigation is to determine the atomic and electron density from our experiments with a dual-wavelength technique. This information was discussed and density values were presented.

Conclusion

5.1 Summary

The overarching purpose of this study was to determine the atomic and electron density of the plasma generated through wire ablation in the PPSL. Following the model proposed by Sarkisov [1], a dual-wavelength interferometric system is presented. The interferometric fringe shifts of two wavelengths are used to estimate the electron and atomic densities.

Utilizing 54 experiments with copper samples, and 9 with aluminum samples, we presented results of plasma evolution to eventual collapse using interferometric techniques in 50-ns intervals. The maximum densities of copper samples are observed to be $N_e = 2.07 \times 10^{18}$ cm^{-3}, and $N_a = 4.56{\times}10^{19}$ cm^{-3}. The maximum densities of aluminum samples are observed to be $N_e = 3.22 \times 10^{18}$ cm^{-3}, and $N_a = 6.15{\times}10^{19}$ cm^{-3}.

In comparing the results to previous work, [1] reported a maximum atomic density of $4.3{\times}10^{19}$ cm^{-3}. It is worth mentioning that [1] used a sample 2-cm in length with equal diameter to our experiments. Sarkisov's wire is twice the length of our sample. Additionally, in [1] their pulsed power source provided 1.5 kA delivered to the sample in 10 ns. In [11], Wu reported a maximum surface atomic density of $1.6{\times}10^{18}$ cm^{-2} using 12 μm diameter, 1 cm long aluminum samples. In [11], the pulsed power source applied 1 kA current over 10 ns, whereas our pulsed power source provided 2.5 kA during the same time duration.

It is clear that it is difficult to directly compare our results to this previous work presented as wire lengths, diameters, composition and pulsed power source are not comparable. Yet, the order of magnitude is comparable. Through continued work, this technique can be developed to be more automated and a complete diagnostic for the PPSL laboratory

5.2 Recommendations and Future Work

After collecting numerous interferograms and evaluating the results, there are many things that could be done differently to improve the time it takes to analyze results and ensure that no data from any interferogram is overlooked. Various recommendations are presented here for improving the work and time to complete the experiments.

First, the sample preparation and set up is critical to achieve repeatable results. A checklist to ensure that each step of the process is completed, would improve procedural efficiency and prevent error caused by inconsistent sample preparation. It is not ideal to load a sample and ablate the wire when the camera was not enabled to take the image. Steps can be made to automate the process through LabView, but every step cannot be automated.

Image smoothing is critical to accurate detection of fringe spacing and fringe shifts. In this effort, we utilized Fourier transform windowing as a technique for image smoothing. This worked well for our analysis, but some errors were noticed at the image corners due to artifacts lost in the process. The necessary window position and size changes throughout our images. After literature review, there are literally hundreds of papers describing efficient and fast methods to perform this task through methods of averaging, edge finding and image enhancement.

Fringe counting is an additional piece that will aid in analysis. When determining the cubic spline fit for fringe re-creation, it was necessary to manually count fringes to determine coefficients. This is because the order of fringes in the upper free space region was different from the fringes in the lower free space region. This was due to fringe curvature.

For example, evaluating the fourth fringe from the left in the upper free space region at 532 nm, would be referenced to the 7th fringe from the left in lower free space. Fringe number is required to consider the cubic spline fit for the same fringe line. An algorithm designed to number the fringes, so that each fringe would not be confused, would make analysis much easier and save tremendous amounts of time.

Automated fringe shift extraction is another technique that would result in improved time savings. Our method requires a cubic spline fit to re-create the original fringe line then measure the number of pixels to the shifted fringe. This was accomplished through mostly manual techniques and only considered one fringe line. In fact, the fringe lines shift a greater distance nearest to the anode and a minimum distance nearest the cathode. We chose to measure nearest to the anode to understand the maximum densities observed during experiment. A technique to scan the images and reconstruct phase shift would yield results for the entire region being observed and provide a more complete data set.

Lastly, the techniques used to determine densities yielded results in line integrated form. This is not a true volumetric density. Able inversion is a technique in which line integrated densities can be converted to a volumetric density. A volumetric result is frequently presented in literature and naturally easier to comprehend the meaning. If more time was available, this technique would have been utilized in our analysis

Bibliography

[1] G. S. Sarkisov, S. E. Rosenthal, K. R. Cochrane, K. W. Struve, C. Deeny, and D. H. McDaniel, "Nanosecond electrical explosion of thin aluminum wires in a vacuum: Experimental and computational investigations," *Physical Review E*, vol. 71, no. 046404, pp. 1–21, 2005.

[2] F. F. Chen, *Introduction to Plasma Physics and Controlled Fusion*. Plenum Press, 1984.

[3] D. A. Frank-Kamenetskii, *Plasma: The Fourth State Of Matter*. Plenum Press, 1972.

[4] L. Zhiwei, B. Weimin, L. Xiaoping, L. Donglin, and Z. Hui, "Influence of plasma pressure fluctuation on RF wave propagation," *Plasma Science and Technology*, vol. 18, pp. 131–137, 2016.

[5] L. Marciniak, A. Wojcik-Gargula, A. Kulinska, J. Bielecki, and U. Wiacek, "Diagnostic systems for the nuclear fusion and plasma research in the PF-24 plasma focus laboratory at the IFJ PAN," *NUKLEONIKA*, vol. 61, pp. 413–418, 2016.

[6] Z. Lin, C. T. Tschang, K. Liao, C. Su, J. Wu, and M. Ho, "Ar/O_2 argon based round atmospheric-pressure plasma jet on sterilizing bacteria and endospores," *IEEE Transaction on Plasma Science*, vol. 44, pp. 3140–3147, 2016.

[7] A. Javid, M. Kumar, and J. G. Han, "Study of sterilization treatment in pure and n-doped carbon thin films synthesized by inductively coupled plasma assisted pulsed-DC magnetron sputtering," *Applied Surface Science*, vol. 392, pp. 1062–1067, 2017.

[8] P. Harihan, *Optical Interferometry*. Academic Press, 1985.

[9] M. Bass, V. Lakshminarayanan, J. Enoch, C. DeCusatis, G. Li, C. MacDonald, E. V. Stryland, and V. Mahajan, *Handbook of Optics*. McGraw Hill, 1995, vol. 1.

[10] P. Harihan, "Selected papers on interferometry." SPIE Optical Engineering Press, 1991, pp. v–ix.

[11] J. Wu, X. Li, Y. Lu, S. V. Lebedev, Z. Yang, S. Jia, and A. Qiu, "Atomization and merging of two Al and W wires driven by a 1 kA, 10 ns current pulse," *Physics of Plasmas*, vol. 23, no. 112703, 2016.

[12] Z. Yang, J. Wu, W. Wei, X. Li, J. Han, S. Jia, and A. Qiu, "Laser-induced plasmas in air studied using two-color interferometry," *Physics of Plasmas*, vol. 23, no. 083523, 2016.

[13] "Interferometry software," http://apre-inst.com/software/, accessed: 2017-02-08.

[14] "ND:YAG laser manufacturer," http://ekspla.com/product/nl120-series-high-energy-slm-q-switched-ndyag-lasers/, accessed: 2017-04-09.

[15] P. Harihan, *Basics of Interferometry*. Elsevier Inc., 2007.

[16] "ND:YAG dichroic mirror," https://www.thorlabs.com/newgrouppage9.cfm?objectgroup_id=7035/, accessed: 2017-04-09.

[17] "CCD Overview," http://www.specinst.com/What_Is_A_CCD.html/, accessed: 2017-04-09.

[18] "Pulse Power Generator," http://www.fidtechnology.com/products/fpg-nanosecond.html/, accessed: 2017-04-09.

[19] "New Wave Tempest 10 ND:YAG Laser," http://pdf.directindustry.com/pdf/new-wave-research/tempest/24449-73372.html, accessed: 2017-04-09.

[20] "FLI Microline series with ML 8300 sensor," https://www.optcorp.com/fli-microline-kaf-8300-monochrome-ccd-camera-with-43mm-high-speed-shutter.html/, accessed: 2017-04-09.

[21] "Berkeley Nucleonics Corporation model 535 signal delay generator," http://www.berkeleynucleonics.com/model-575/, accessed: 2017-04-09.

[22] "HP Infinium model 54845A oscilloscope," http://www.keysight.com/en/pd-1000001468%3Aepsg%3Apro-pn-54845A/4-channel-15-ghz-8-gsa-s-infiniium-oscilloscope?cc=US&lc=eng, accessed: 2017-04-09.

[23] T. S. Bastian, "Notes on electromagnetic waves in a plasma," *National Radio Astronomy Observatory*, 2005.

[24] S. A. Pikuz, V. M. Romanova, N. Baryshnikov, M. Hu, B. R. Kusse, D. B. Sinars, T. A. Shelkovenko, and D. A. Hammer, "A simple air wedge shearing interferometer for studying exploding wires," *Review of Scientific Instruments*, vol. 72, no. 1, 2011.

[25] M. Born and E. Wolf, *Principles of Optics*, 7th ed. Cambridge University Press, 1999.

[26] G. Sarkisov, I. Beigman, V. Shevelko, and K. Struve, "Interferometric measurements of dynamic polarizabilities for metal atoms using electrically exploding wires in a vacuum," *Physical Review A*, vol. 73, 2006.

[27] “Copper and aluminum densities,” https://www.physics.nist.gov/cgi-bin/Star/compos.pl?matno=029/, accessed: 2017-04-26.

[28] “Critical Values of the Student’s t Distribution,” http://www.itl.nist.gov/div898/handbook/eda/section3/eda3672.html, accessed: 2017-04-28.

Appendix A: Interferogram Sequence

Listed below are the interferograms collected during this effort from 0 to 600ns.

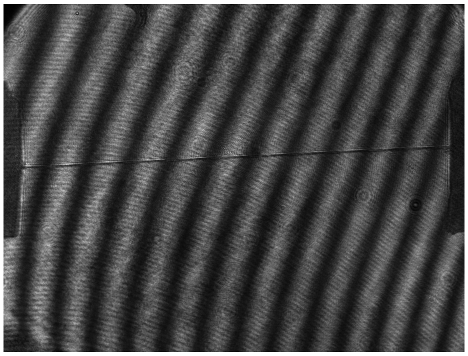

1064 nm 0 ns

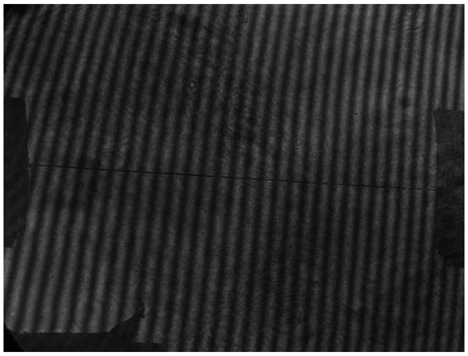

532 nm 0 ns

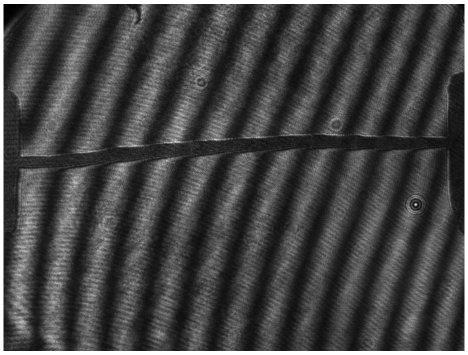

1064 nm 50 ns

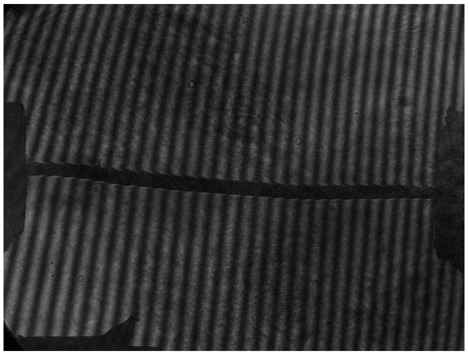

532 nm 50 ns

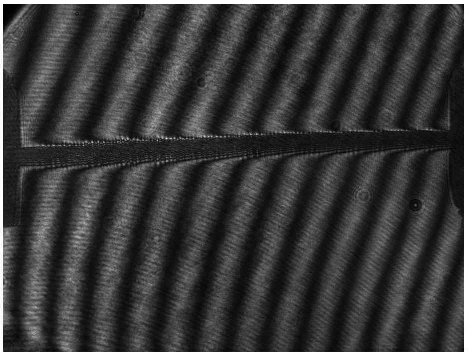

1064 nm 100 ns

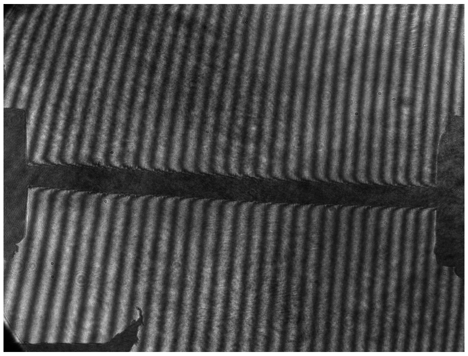

532 nm 100 ns

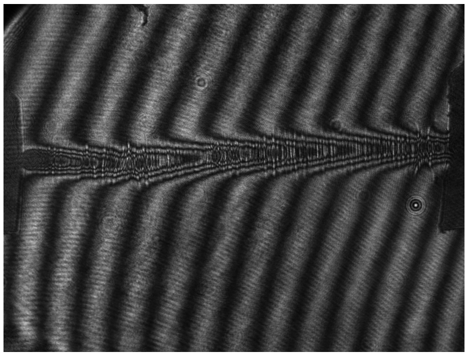

1064 nm 150 ns

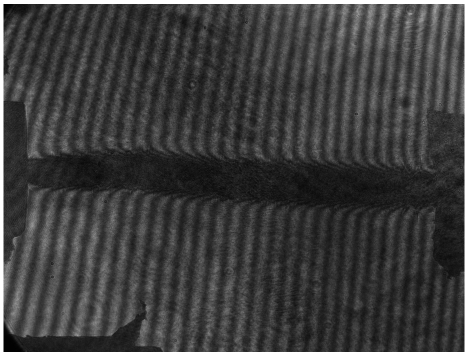

532 nm 150 ns

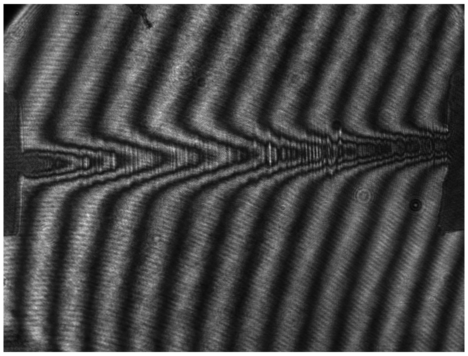

1064 nm 200 ns

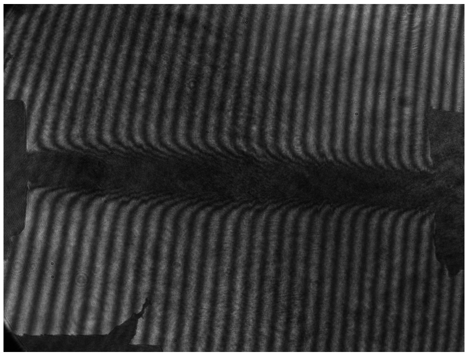

532 nm 200 ns

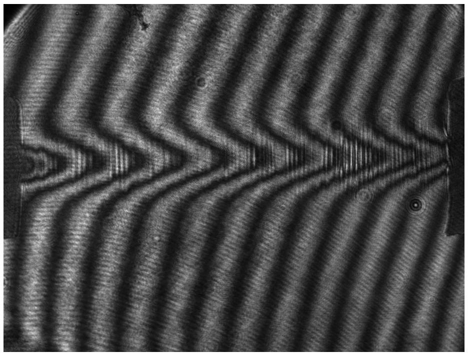

1064 nm 250 ns

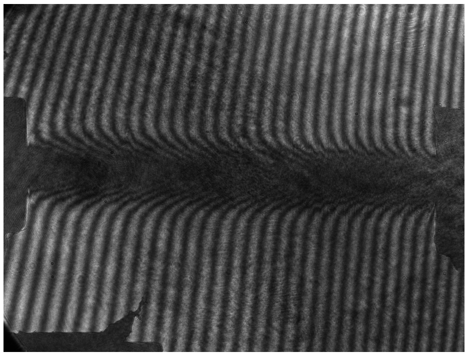

532 nm 250 ns

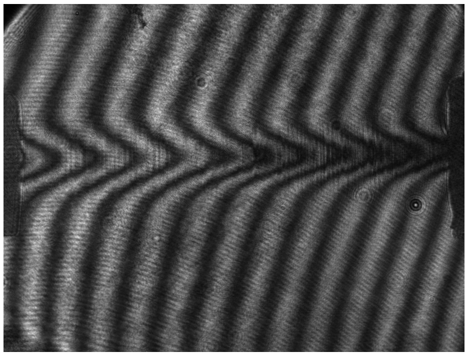

1064 nm 300 ns

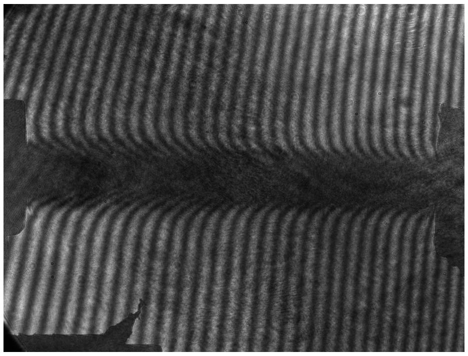

532 nm 300 ns

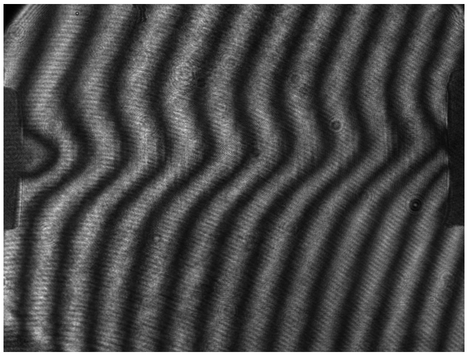

1064 nm 350 ns

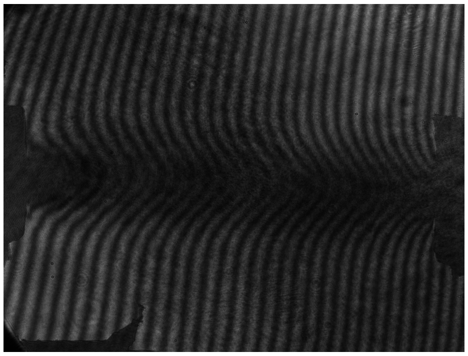

532 nm 350 ns

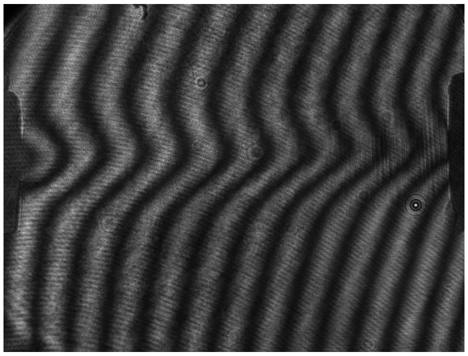

1064 nm 400 ns

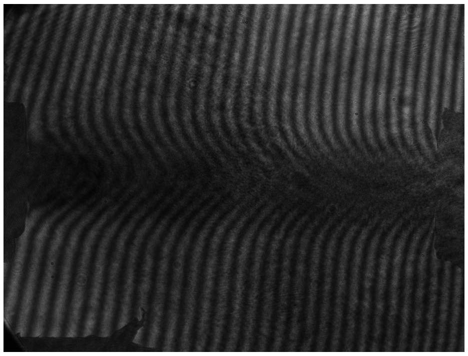

532 nm 400 ns

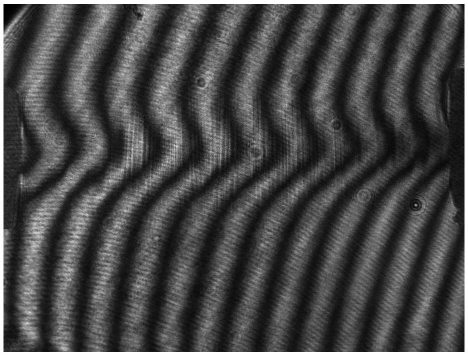

1064 nm 450 ns

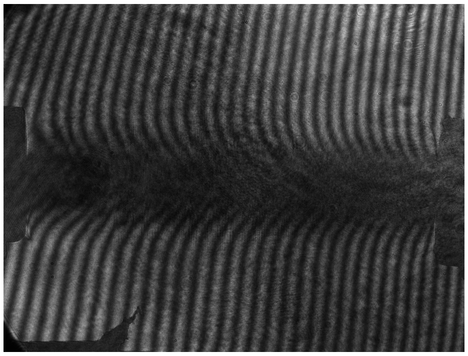

532 nm 450 ns

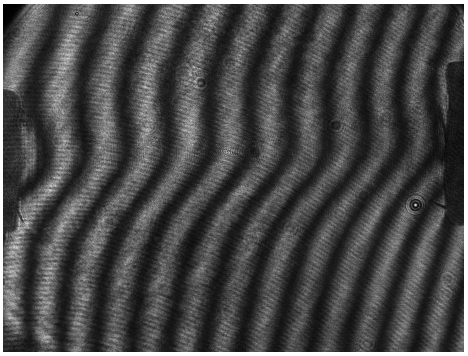

1064 nm 500 ns

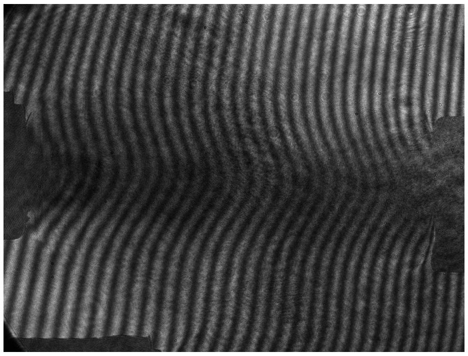

532 nm 500 ns

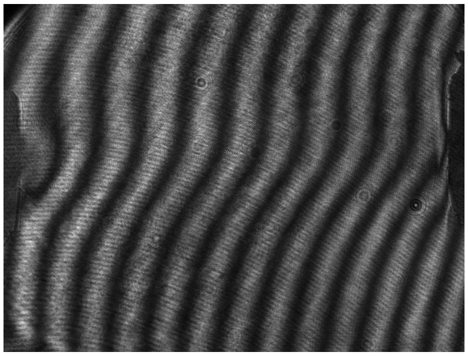

1064 nm 550 ns

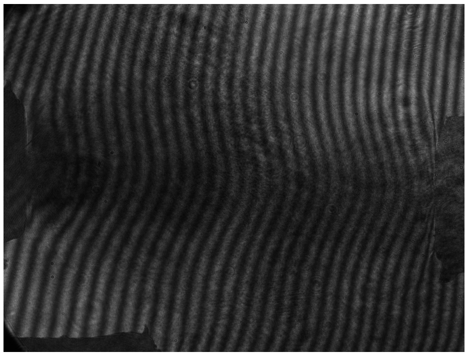

532 nm 550 ns

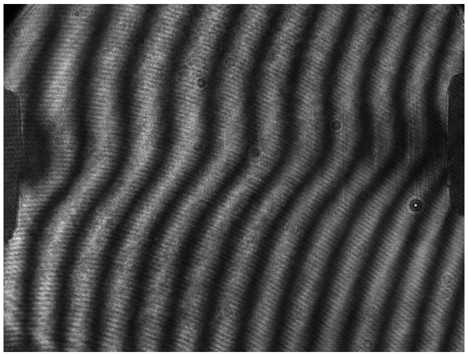

1064 nm 600 ns

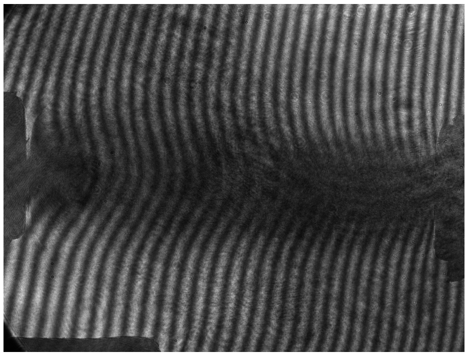

532 nm 600 ns

Appendix B: Duplicate Interferograms

The figures below were collected to represent the repeatability of shots. At each increment of 150 ns, an additional 6 experiments were completed.

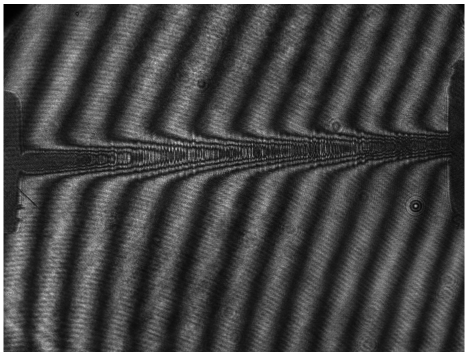

1064 nm 150 ns

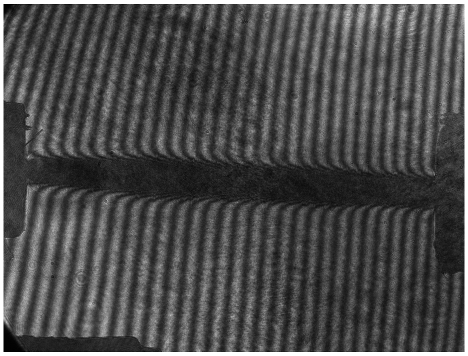

532 nm 150 ns

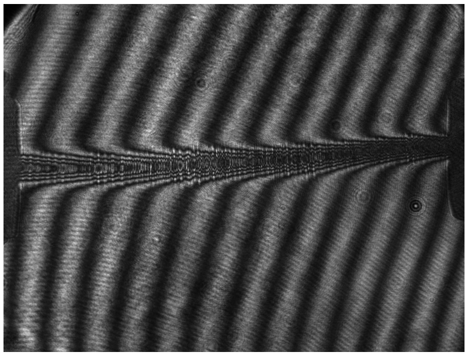

1064 nm 150 ns

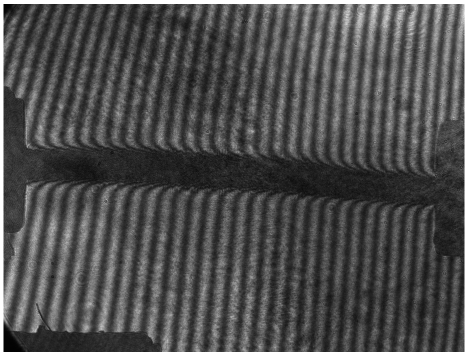

532 nm 150 ns

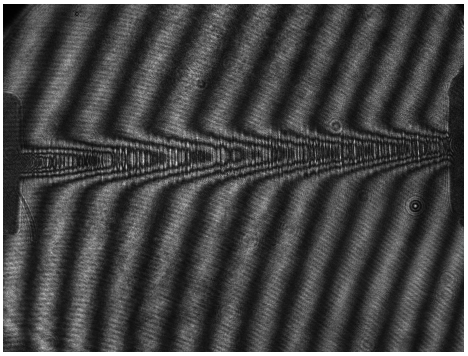

1064 nm 150 ns

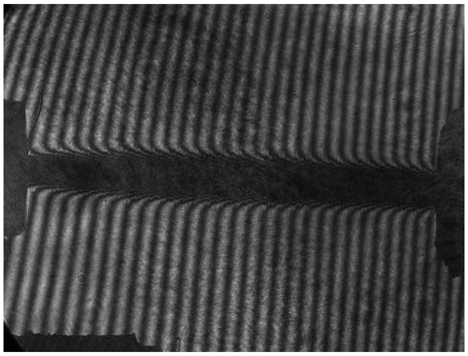

532 nm 150 ns

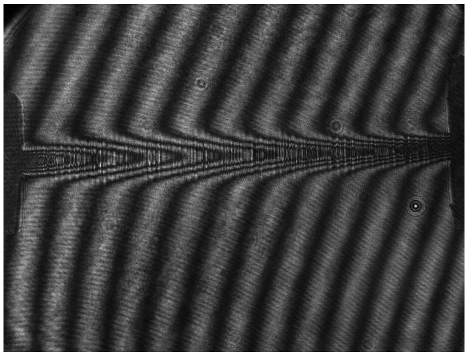

1064 nm 150 ns

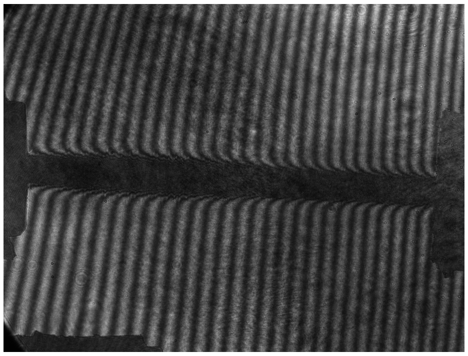

532 nm 150 ns

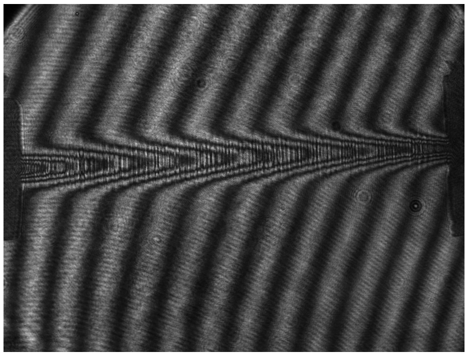

1064 nm 150 ns

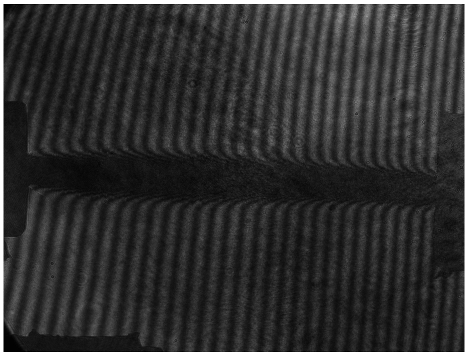

532 nm 150 ns

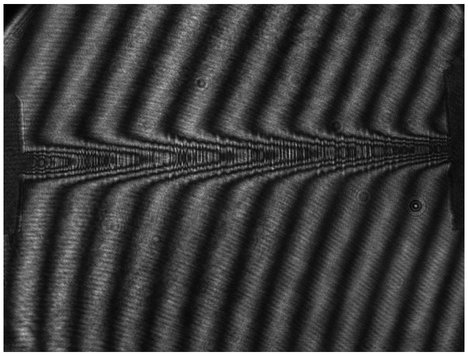

1064 nm 150 ns

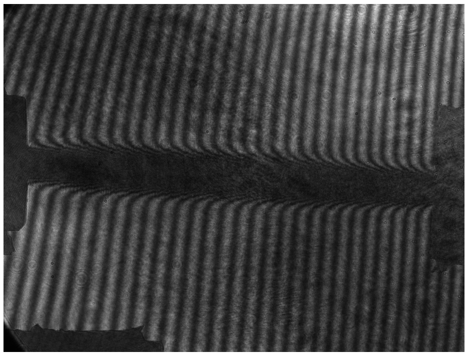

532 nm 150 ns

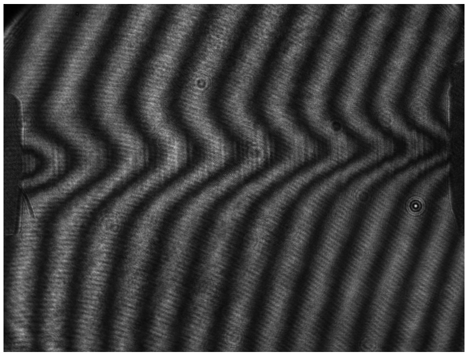

1064 nm 300 ns

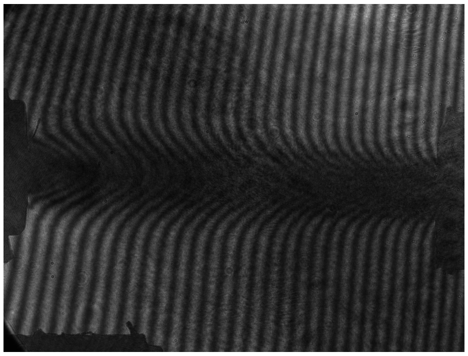

532 nm 300 ns

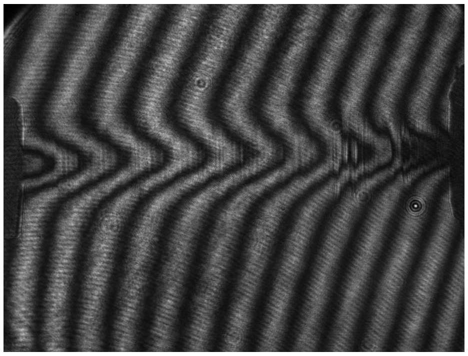

1064 nm 300 ns

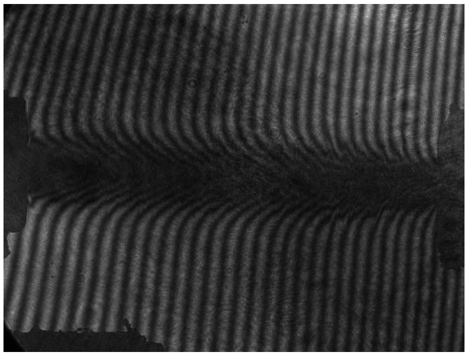

532 nm 300 ns

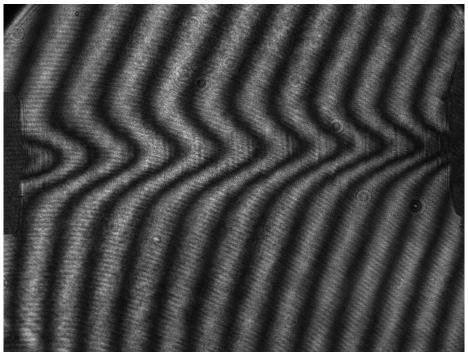

1064 nm 300 ns

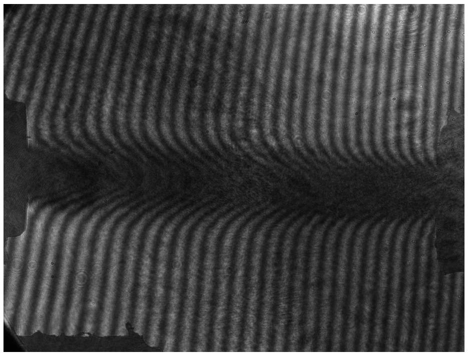

532 nm 300 ns

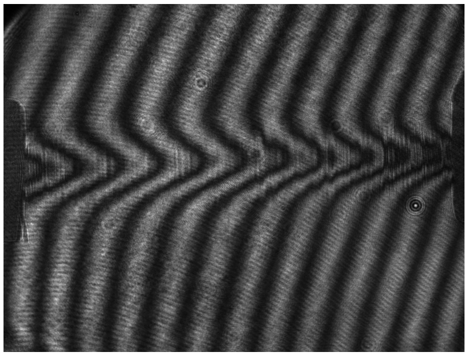

1064 nm 300 ns

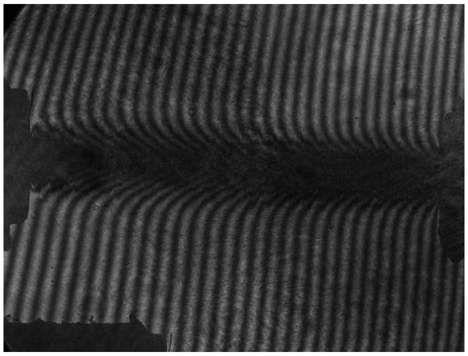

532 nm 300 ns

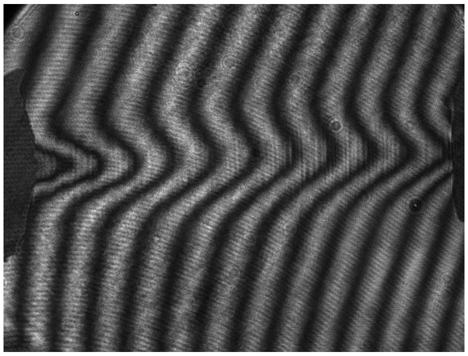

1064 nm 300 ns

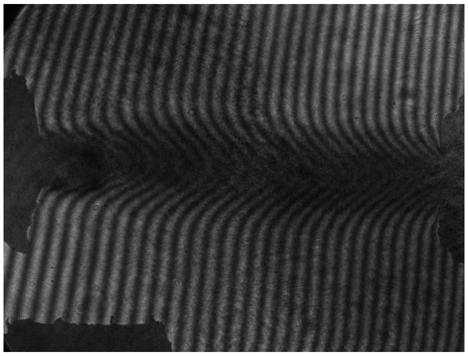

532 nm 300 ns

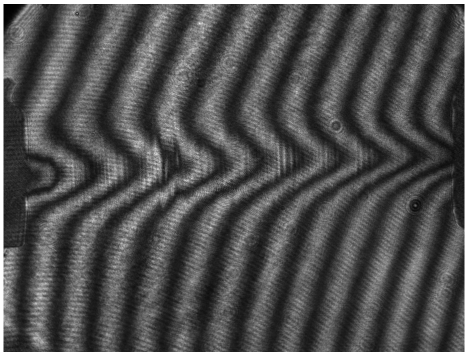

1064 nm 300 ns

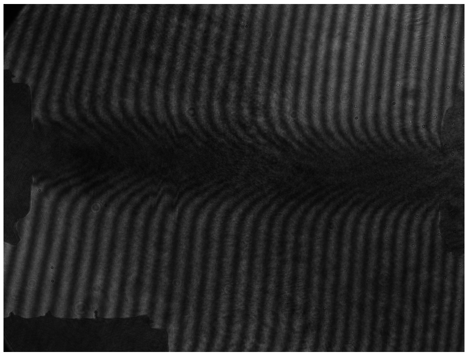

532 nm 300 ns

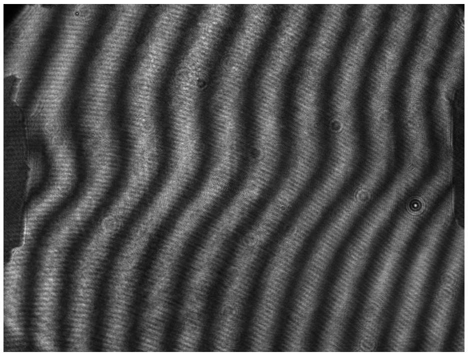

1064 nm 450 ns

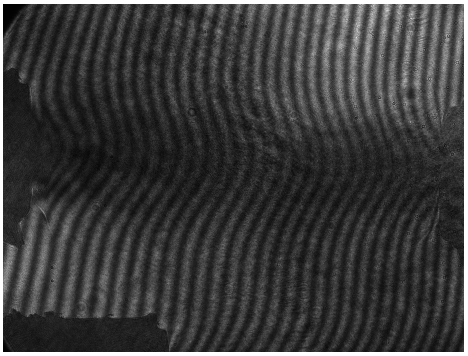

532 nm 450 ns

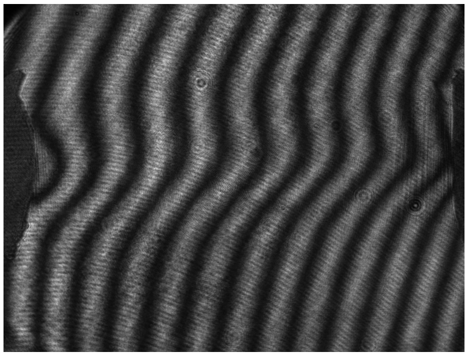

1064 nm 450 ns

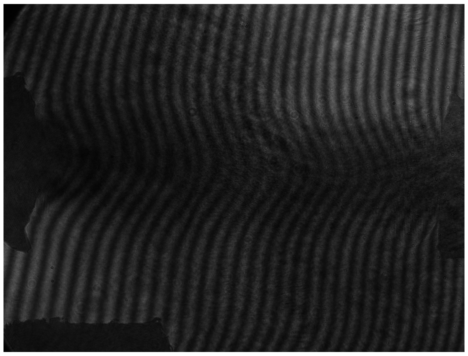

532 nm 450 ns

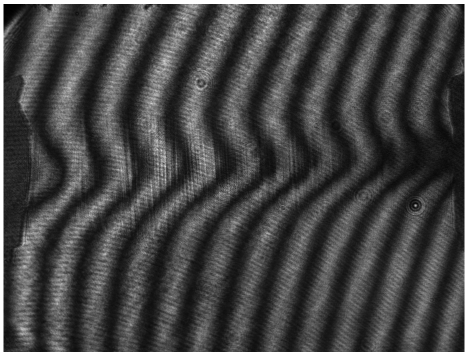

1064 nm 450 ns

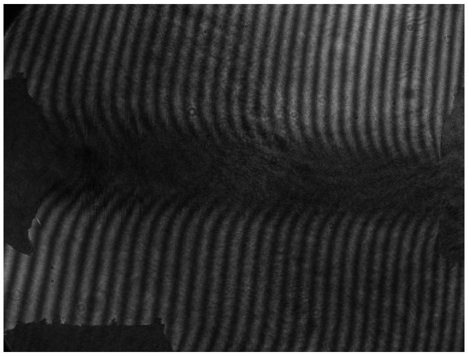

532 nm 450 ns

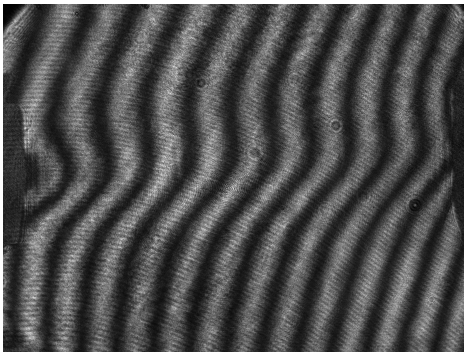

1064 nm 450 ns

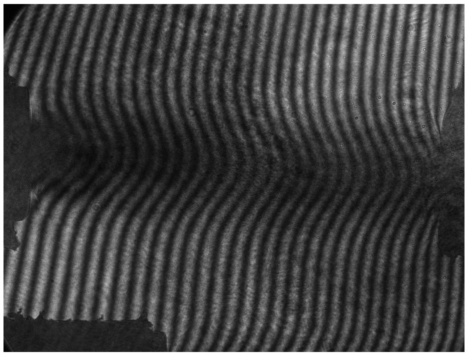

532 nm 450 ns

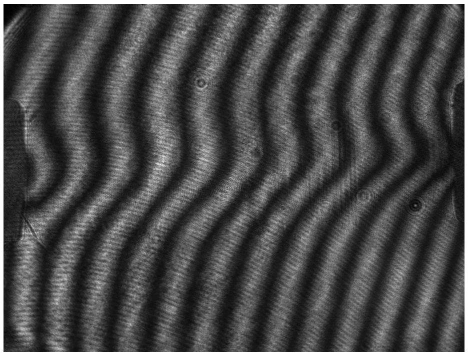

1064 nm 450 ns

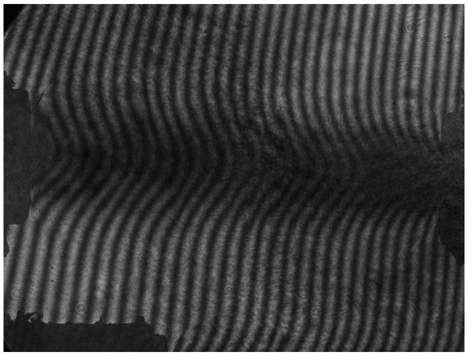

532 nm 450 ns

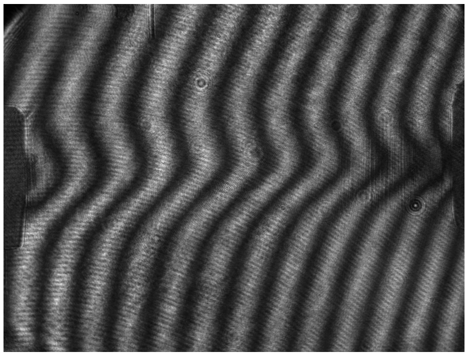

1064 nm 450 ns

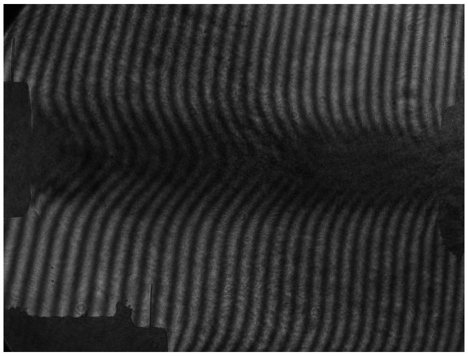

532 nm 450 ns

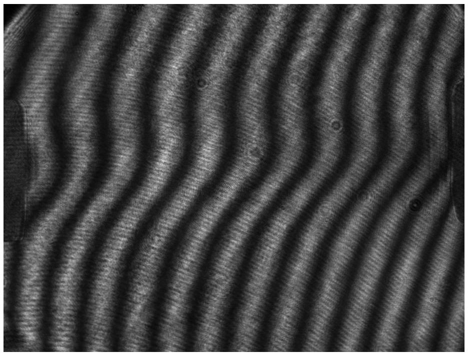

1064 nm 600 ns

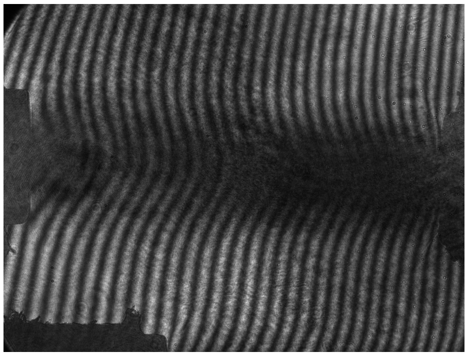

532 nm 600 ns

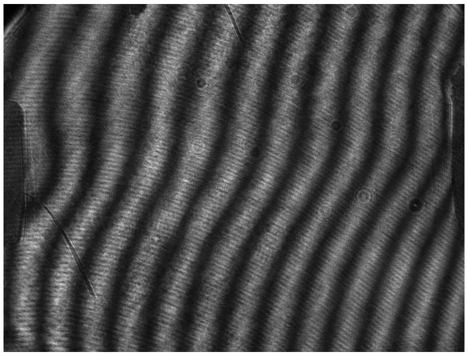

1064 nm 600 ns

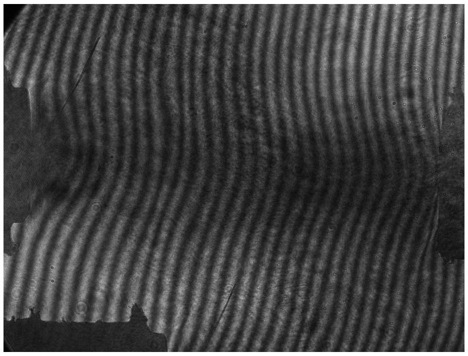

532 nm 600 ns

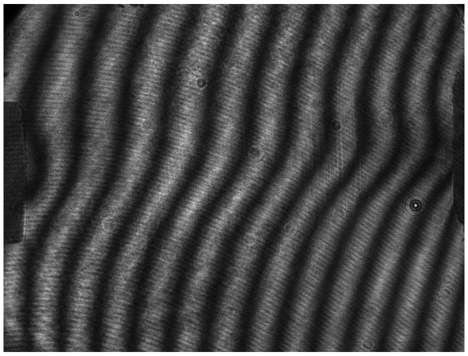

1064 nm 600 ns

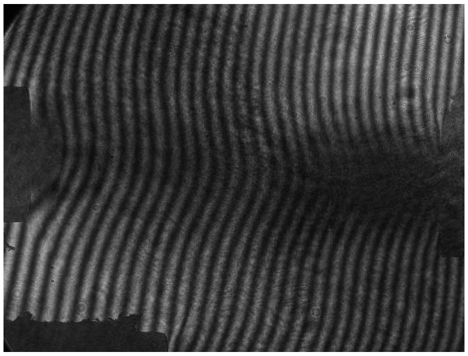

532 nm 600 ns

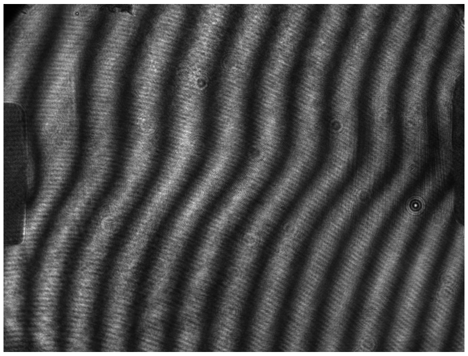

1064 nm 600 ns

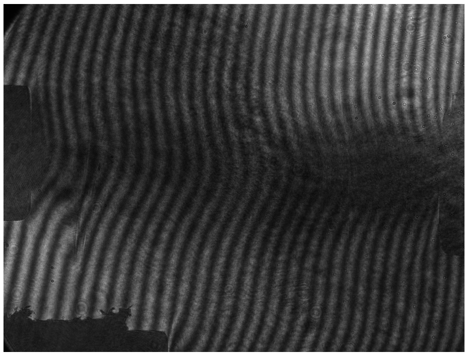

532 nm 600 ns

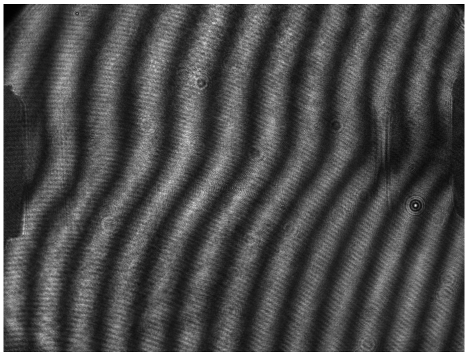

1064 nm 600 ns

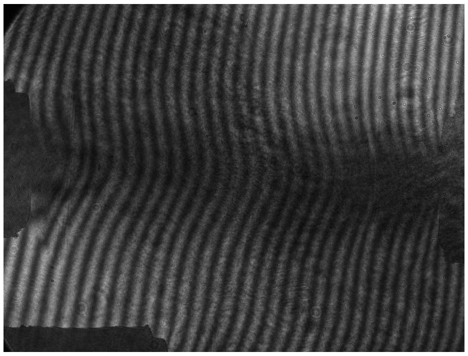

532 nm 600 ns

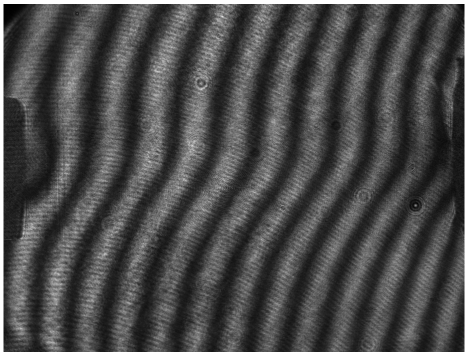

1064 nm 600 ns

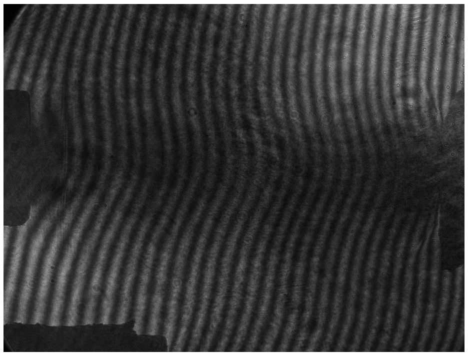

532 nm 600 ns